arXiv:1209.6055v1 [astro-ph.CO] 26 Sep 2012

Mid-Infrared Selection of Active Galactic Nuclei with the Wide-Field Infrared Survey Explorer. II. Properties of WISE-Selected Active Galactic Nuclei in the NDWFS Boötes Field

R.J. Assef[1,2], D. Stern[1], C.S. Kochanek[3,4], A.W. Blain[5], M. Brodwin[6], M.J.I. Brown[7], E. Donoso[8], P.R.M. Eisenhardt[1], B.T. Jannuzi[9], T.H. Jarrett[8], S.A. Stanford[10,11], C.-W. Tsai[8], J. Wu[1,2], L. Yan[8]

ABSTRACT

Stern et al. (2012) presented a study of WISE selection of AGN in the 2 deg^2 COSMOS field, finding that a simple criterion W1–W2$\geq$0.8 provides a highly reliable and complete AGN sample for W2$<$15.05, where the W1 and W2 passbands are centered at 3.4μm and 4.6μm, respectively. Here we extend this study using the larger 9 deg^2 NOAO Deep Wide-Field Survey Boötes field which also has considerably deeper WISE observations than the COSMOS field, and find that this simple color-cut significantly loses reliability at fainter fluxes. We define a modified selection criterion combining the W1$-$W2 color and the W2 magnitude to provide highly reliable or highly complete AGN samples for fainter WISE

[1]Jet Propulsion Laboratory, California Institute of Technology, 4800 Oak Grove Drive, Mail Stop 169-236, Pasadena, CA 91109, USA. E-mail: roberto.j.assef@jpl.nasa.gov

[2]NASA Postdoctoral Program Fellow

[3]Department of Astronomy, The Ohio State University, 140 W. 18th Ave., Columbus, OH 43210, USA

[4]The Center for Cosmology and Astroparticle Physics, The Ohio State University, 191 West Woodruff Avenue, Columbus, OH 43210, USA

[5]Physics & Astronomy, University of Leicester, 1 University Road, Leicester, LE1 7RH, UK

[6]Department of Physics, University of Missouri, 5110 Rockhill Road, Kansas City, MO 64110, USA

[7]School of Physics, Monash University, Clayton 3800, Victoria, Australia

[8]Infrared Processing and Analysis Center, California Institute of Technology, Pasadena, CA 91125, USA

[9]Steward Observatory, University of Arizona, Tucson, AZ 85721, USA

[10]Department of Physics, University of California, One Shields Avenue, Davis, CA 95616, USA

[11]Institute of Geophysics and Planetary Physics, Lawrence Livermore National Laboratory, Livermore, CA 94550, USA

sources. In particular, we define a color-magnitude cut that finds 130±4 deg^{-2} AGN candidates for W2<17.11 with 90% reliability. Using the extensive UV through mid-IR broad-band photometry available in this field, we study the spectral energy distributions of WISE AGN candidates. As expected, the WISE AGN selection is biased towards objects where the AGN dominates the bolometric luminosity output, and that it can identify highly obscured AGN. We study the distribution of reddening in the AGN sample and discuss a formalism to account for sample incompleteness based on the step-wise maximum-likelihood method of Efstathiou et al. (1988). The resulting dust obscuration distributions depend strongly on AGN luminosity, consistent with the trend expected for a Simpson (2005) receding torus. At $L_{\rm AGN} \sim 3 \times 10^{44}$ erg s^{-1}, 29±7% of AGN are observed as Type 1, while at $\sim 4 \times 10^{45}$ erg s^{-1} the fraction is 64±13%. The distribution of obscuration values suggests that dust in the torus is present as both a diffuse medium and in optically thick clouds.

Subject headings: galaxies: active — methods: statistical — quasars: general

1. Introduction

Active galactic nuclei (AGN) have been proposed to play an important role in several aspects of galaxy evolution, such as quenching star-formation in their host galaxies by heating and/or mechanically pushing their gas reservoirs into the intergalactic medium (see, e.g., Hopkins et al. 2005), preventing cooling flows at the center of galaxy clusters (see, e.g., Croton et al. 2006), and possibly by contributing significantly to the reionization of the Universe at high redshift (Glikman et al. 2010, 2011). Efficiently identifying AGN in all states of accretion and obscuration and accurately understanding their properties and structure is a key step to understand how galaxies evolve with cosmic time.

AGN are among the most luminous objects in the Universe. While the bulk of the soft X-ray through NIR luminosity is thought to be thermally produced near the central super-massive black hole (SMBH) in an accretion disk (e.g., Shakura & Sunyaev 1973), a considerable fraction of this luminosity is absorbed by dust surrounding the SMBH on parsec scales, and re-radiated in the mid-IR. This dust is generally believed to be responsible for the Type 1/2 dichotomy (see, e.g., Antonucci 1993). The dust distribution is typically thought to have a quasi-toroidal shape (see, e.g., Urry & Padovani 1995), with a scale height and opening angle that depends on the luminosity of the accretion disk (see, e.g., Simpson 2005). Because the dust is hot, at temperatures reaching its sublimation limit ($\sim$ 1500K), the emission is enhanced and much redder than the Rayleigh-Jeans tail in the 3 to 10μm range

(see, e.g., Stern et al. 2005). Hence, even if dust in the torus is blocking our line of sight towards the SMBH and absorbing the soft X-rays through NIR emission of the accretion disk, the distinctive mid-IR warm dust emission from the torus is still observable.

The Wide-field Infrared Survey Explorer (WISE; Wright et al. 2010) is a NASA satellite with a 40cm aperture that imaged the whole sky in four mid-IR bands, centered at 3.4, 4.6, 12 and 22μm. We refer to these bands as W1, W2, W3 and W4, respectively. The fully cryogenic WISE science mission started in January 2010 and ended in August of the same year; all of this data has been publicly available since March 2012. While not one of its main goals, WISE is well suited to studying AGN as its bands are sensitive to their characteristic warm dust emission and are little affected by the obscuration expected from either the dust in the torus or in the interstellar medium of the host galaxy. In a companion work, Stern et al. (2012, Paper I) investigated the power of WISE to identify AGN based solely on the W1–W2 mid-IR color by comparing to known AGN in the COSMOS field. The selection also necessarily entails a flux cut, which is relatively shallow given the low ecliptic latitude of the COSMOS field and thus lower WISE coverage depth. Using a set of AGN in the field selected from the *Spitzer* Infrared Array Camera (IRAC; Fazio et al. 2004) colors according to the criteria developed by Stern et al. (2005) as a control sample, we determined that at the depth of the COSMOS field a very simple selection criterion of W1$-$W2$\geq$0.8 and W2$<$15.05 produced an AGN sample with a contamination of only 5% and recovered nearly 80% of the IRAC-selected AGN in the field to that WISE depth. The 61.9 ± 5.4 deg^{-2} space density of these AGN is about three times higher than that of similar bolometric luminosity Type 1 AGN found at optical wavelengths by the Sloan Digital Sky Survey (SDSS; Richards et al. 2002). The color of this criterion is similar to that proposed earlier by Assef et al. (2010, W1–W2$>$0.85) using mock WISE data constructed from SED models calibrated in this wavelength range by *Spitzer* data. Assef et al. (2010) have shown that WISE and SDSS are sensitive to AGN of the same bolometric luminosities for $z < 4$, implying that the increased census is due to the sensitivity of WISE to those objects obscured by dust. In fact, Paper I showed that the distribution of the X-ray hardness ratios of the WISE-selected AGN are, as expected, consistent with a considerable number of dust-obscured AGN.

Because of the orbit and observing strategy of WISE, the depth of a field depends strongly on ecliptic latitude. The 2 deg^2 COSMOS field, close to the ecliptic, is representative of the shallowest WISE fields. In this work we extend the work presented in Paper I to the much larger, 9 deg^2 NOAO Deep Wide-Field Survey (NDWFS; Jannuzi & Dey 1999) Boötes field, which has considerably deeper WISE observations due to its higher ecliptic latitude. In §2 we describe the data sets and spectral energy distribution (SED) fitting models which we use to extend the AGN selection criteria of Paper I to fainter WISE fluxes in §3. In §4 we study the broad-band SEDs of the WISE AGN candidates, and assess the accuracy

with which we can estimate photometric redshifts for them. Finally, in §5, we study the distribution of the obscuring dust in AGN and present a method to correct for sample incompleteness due to reddening. Throughout this work we assume a flat ΛCDM cosmology with $H_0 = 73$ km s^{-1}, $\Omega_M = 0.3$ and $\Omega_\Lambda = 0.7$. We refer to all magnitudes in their native photometric system, i.e., AB for *ugriz*, FUV and NUV, and A0 (Vega) for all other bands.

2. Data and Modeling

2.1. The NOAO Deep Wide-Field Survey Boötes Field

NDWFS is a deep imaging survey in B_W, R, I and K of two 9 deg^2 fields in the constellations of Cetus and Boötes. We focus here on the Boötes field, for which follow-up deep imaging has been obtained for a wide range of wavelengths. Boötes also has deep and extensive spectroscopy.

Follow-up imaging of the Boötes field exists from the X-rays with Chandra (XBoötes; Murray et al. 2005) to the radio from the Faint Images of the Radio Sky at Twenty-centimeters (FIRST; Becker et al. 1995) survey, the NRAO VLA Sky Survey (NVSS; Condon et al. 1998), the Westerbork Northern Sky Survey (WENSS; Rengelink et al. 1997) and from de Vries et al. (2002). The whole field was observed with 90 seconds of exposure per position in the IRAC Shallow Survey (Eisenhardt et al. 2004). The Spitzer Deep, Wide-Field Survey (SDWFS; Ashby et al. 2009) quadrupled this exposure, reaching 5σ depths of 19.3, 18.5, 16.3 and 15.6 mag for [3.6], [4.5], [5.8] and [8.0], respectively. Additionally, we also use the Galaxy Evolution Explorer (*GALEX*; Martin et al. 2005) Deep Imaging Survey (DIS) and All-sky Imaging Survey (AIS) FUV and NUV observations of the field, the z-band data of Cool (2007), the near-IR J, H and K_s observations of NEWFIRM (Gonzalez et al. 2010) and the MIPS 24μm observations of the MIPS AGN and Galaxy Evolution Survey (MAGES; Jannuzi et al. 2010). For our work, we use $6''$ aperture magnitudes, corrected for PSF losses, obtained from PSF-matched images in all but the *Spitzer* bands.

The AGN and Galaxy Evolution Survey (AGES; Kochanek et al. 2012) obtained deep optical spectra of approximately 25,000 sources in the Boötes field with Hectospec (Fabricant et al. 2005) at the Multiple Mirror Telescope (MMT). The survey is designed to be statistically complete for several different samples limited to $I < 20$ for galaxy candidates and $I < 22.5$ for AGN candidates. AGES is highly complete for AGN candidates to $I < 21.5$. The AGN candidates were targeted by their X-ray, radio and mid-IR properties, but not by their optical colors. This ensures that none of the optical selection biases (see, e.g., Fan 1999) are propagated into the sample. We complement the AGES spectroscopy with ~ 2000 deeper optical

spectra from various sources, primarily from Keck (e.g., Eisenhardt et al. 2008). Since these data do not have a uniform selection function, they will only be of limited use in our analysis.

2.2. WISE Observations

The WISE mission observed the full sky in four mid-IR photometric bands with FWHM of 6″ in W1–3 and 12″ in W4. We use the WISE all-sky data release, which includes all observations obtained during the fully cryogenic mission. WISE surveyed the sky in a polar orbit with respect to the ecliptic, simultaneously obtaining images in all four bands. Hence, the number of observations in a field increases with its ecliptic latitude. While fields near the ecliptic were typically observed 12 times, the number can grow to several hundreds near the ecliptic poles (e.g., Jarrett et al. 2011). The median coverage across the sky is approximately 15 frames per passband. In particular, the COSMOS field was observed with a median coverage of 11 frames per passband, well below the median sky coverage. Detailed accounts of the mission are presented by Wright et al. (2010) and in the WISE all-sky data release explanatory supplement[1].

The NDWFS Boötes field is at an ecliptic latitude of 46 deg, and hence WISE obtained an average coverage of 30 frames in each band, reaching 10σ depths in W1, W2, W3 and W4 of approximately 17.12 mag, 15.73 mag, 11.55 mag and 7.83 mag. For all sources, we use fluxes obtained through profile fitting. We limit the sample to $S/N > 3$ in W1 and W2, or equivalently to W1<18.50 and W2<17.11. We match to other sources in Boötes by finding the closest IRAC [4.5] source within 2″ with the constraint that no WISE (IRAC) source is matched to more than one IRAC (WISE) source. This results in a sample of 111,720 matched sources. We note that the WISE magnitude limit is applied after cross-matching with the IRAC sources.

Detailed comparison between WISE and *Spitzer* IRAC photometry has shown that WISE profile-fitting fluxes are typically underestimated for faint sources, and that the magnitude of the effect increases with decreasing IRAC flux, reaching offsets of a few tenths of a magnitude for the fainter sources (see section VI.3 of the WISE all-sky data release explanatory supplement for details). While there is no simple prescription to mitigate it, this bias is unlikely to affect the results of our SED fits, as it is only significant for faint sources for which the deeper IRAC SDWFS magnitudes dominate the χ^2 of the fit in the mid-IR. Because of this, we do not attempt to compensate for this WISE calibration issue in our study.

[1] `http://wise2.ipac.caltech.edu/docs/release/allsky/expsup/`

2.3. Spectral Energy Distribution Modeling

We rely on SED modeling both to obtain physical insight into our AGN candidates, and to obtain photometric redshift ($z_{\rm phot}$) estimates for all objects without available spectroscopic redshifts. To fit the SEDs we use the non-negative basis of low-resolution, UV through mid-IR SED templates for AGN and galaxies of Assef et al. (2010). The basis consists of four empirically derived SED templates, where every object is modeled as a non-negative combination of the three galaxy SED templates (roughly corresponding to E, Sbc and Im types) and the single AGN template. For the AGN template alone, we allow reddening with a strength parametrized by $E(B-V)$. For high-redshift sources, we model the intergalactic medium (IGM) absorption following Fan et al. (2006) for Lyα and Lyβ absorption and Stengler-Larrea et al. (1995) for Lyman limit systems. The strength of the IGM absorption can also be fit beyond the standard mean absorption law, although this extra degree of freedom often has a negative impact on the accuracy of photometric redshifts. A weak prior is used to keep $E(B-V)$ as small as possible with the secondary effect that obscuration values may be slightly underestimated in some cases. We refer the reader to Assef et al. (2010) for further details.

We follow the prescription detailed in Assef et al. (2010) to obtain photometric redshifts and fit the SEDs. Since photometric redshifts using 24μm photometry have lower accuracies when using these templates (see Assef et al. 2010, for details), we derive photometric redshifts for all objects in the sample using only the broad-band photometry from FUV to W3. Adding MIPS 24μm and W4 photometry, however, does not qualitatively alter our results. We assume the standard mean IGM absorption and use a luminosity prior for the galaxy components based on the Las Campanas Redshift Survey (LCRS) $r-$band luminosity function (Lin et al. 1996). We discuss the precision of the photometric redshifts in §4.1.

After obtaining photometric redshift estimates, we re-fit the SEDs of all objects now including the W4 and MIPS 24μm channels, and also fit for the strength of the IGM absorption. Whenever possible, we use spectroscopic redshifts ($z_{\rm spec}$). This approach ensures that we get the best SED model possible for each object. Several authors have determined that photometric redshifts for Type 1 AGN obtained solely with broad-band filter photometry can be wildly inaccurate (see, e.g., Rowan-Robinson et al. 2008; Salvato et al. 2009; Assef et al. 2010); this is discussed further in §4.1 in the context of our study. However, our spectroscopic data is particularly deep and complete for AGN (see §2.1), somewhat mitigating this issue.

In order to reliably separate AGN from inactive galaxies, we use the parameter

$$\hat{a} \equiv \frac{L_{\rm AGN}}{L_{\rm host} + L_{\rm AGN}}, \tag{1}$$

where the luminosities correspond to the integrated specific luminosities of the best-fit templates over the 0.1 and 30μm wavelength range for the AGN template and 0.03 to 30 μm for the host galaxy templates (see Assef et al. 2010, for details). The specific luminosities are calculated after correcting the AGN component for reddening. We refer to these as bolometric luminosities for the rest of the paper. Note that Assef et al. (2010) determined that $\hat{a}$ is insensitive to photometric redshift uncertainties as long as enough data exists to constrain the fit, in the sense that $\hat{a}$ can still be accurately determined for objects where reliable photometric redshifts cannot be measured. That is to say, while it is challenging to measure accurate photometric redshifts for AGN, particularly for Type 1 AGN, we are able to accurately disentangle the relative fractions of starlight and nuclear emission even when the redshift estimate is significantly in error.

3. WISE AGN Color Selection

In this section we study the completeness and reliability of WISE AGN selection. First, we discuss the criterion of Paper I applied to the deeper WISE data in the Boötes field, while in §3.2 we improve our method by also considering the observed W2 magnitude of the sources. In §3.3 we compare our new method with others in the literature.

3.1. Magnitude-Independent AGN Color Selection

In Paper I we investigated the distribution of quasars in WISE color space in the COSMOS survey field. We found that for objects with W2<15.05 mag (W2 $S/N \geq 10$ at that ecliptic latitude), the simple color cut based on the two shortest wavelength WISE bands

$$\mathrm{W1} - \mathrm{W2} \ \geq \ 0.8, \tag{2}$$

provides an effective criterion to separate AGN from inactive galaxies. When compared to the IRAC color selection method of Stern et al. (2005, see Assef et al. 2010 for discussion about its reliability), the WISE color criterion selection recovers 78% of the IRAC-selected AGN with a 95% reliability. Notably, six of the AGN candidates selected by IRAC and WISE were not detected in the 1.8Ms Chandra survey of the COSMOS field (C-COSMOS; Elvis et al. 2009), suggesting they may be Compton-thick (see Paper I for details). The reason behind the success of this criterion is clearly illustrated in Figure 1. This figure shows mid-IR color as a function of redshift for the AGN and galaxy SED templates of Assef et al. (2010). For $z \lesssim 3$, the W1–W2 color of unobscured AGN is well above the color cut of 0.8 mag. At higher redshift, reddened AGN ($E(B-V) \gtrsim 0.4$) can also be redder than this

color cut. In practice, however, it is exceedingly uncommon to find high redshift, highly reddened AGN bright enough to be detected by WISE and so much more luminous that their host galaxy to dominate the rest-frame optical emission. Indeed, in Paper I we found no quasars with $z > 3$ in the sample. We also find very few galaxies with $z \gtrsim 1$, since the WISE observations of the COSMOS field are not deep enough to find normal galaxies at high redshifts. While other populations such as some ULIRGs and brown-dwarfs can have even redder W1–W2 colors, they are too rare in comparison to AGN to be a significant source of contamination. Note that Figure 1 implies that this W1–W2 color selection is biased against AGN which are faint with respect to their host galaxies. If the flux in the WISE bands is dominated by the galaxy, the colors will drop below the selection limit, moving towards the galaxy locus at $\mathrm{W1} - \mathrm{W2} \sim 0$. We discuss this further in §4.3.

The criteria of Paper I are readily applicable to the all-sky WISE survey, and are demonstrated to be both reliable and complete to the shallow depth of the WISE observations of the COSMOS field. However, due to the limited size of that field, it does not have the statistical power to address many interesting and pressing issues in AGN studies, such as AGN evolution, accretion rates, and dust distributions. More importantly, since most of the WISE survey area has deeper coverage than in the COSMOS field, alternative selection criteria are valuable for a census of WISE-selected AGN in these deeper regions. Jarrett et al. (2011) has shown that in the deepest WISE fields at the ecliptic poles, where W1 and W2 are confusion limited, the addition of W3 is a very useful aid in the identification of AGN. Our intention is to bridge these two extremes, proposing a robust WISE AGN selection technique for fields with intermediate depth.

In order to extend the study of Paper I, we turn to the NDWFS Boötes field, which helps with both issues highlighted above: it has a WISE median coverage of 30 frames, almost three times that of COSMOS, and extends over 9 deg^2, an area 4.5 times larger. We start by replicating the selection criterion of Paper I in the Boötes field, but up to the W2 10σ depth provided by the full co-added data. While this implies a sample 0.68 mag deeper, it maintains the error properties of the sample and so provides a meaningful comparison.

The left panel of Figure 2 shows the WISE color distribution of sources in our sample. Comparing to sources selected as AGN by their IRAC colors (Stern et al. 2005), we find that a simple $\mathrm{W1}-\mathrm{W2}\geq 0.8$ color cut identifies 70% of the IRAC-selected AGN with 70% reliability. Compared to applying this cut at the 10σ WISE depth of COSMOS as reported in Paper I, the drop in completeness is relatively small, from 78% to 70%. The decrease in reliability from 95% to 70% is very significant, however, and is simply due to the modest increase in field depth. If we limit the Boötes field analysis to the 10σ W2 level of the COSMOS field (W2<15.05, right panel of Fig. 2), we recover similar AGN demographics to

that reported in Paper I, with 78% completeness and 94% reliability.

The lower completeness means an increase in IRAC-selected AGN detected but not identified by the simple WISE color criterion. This is likely due to a combination of (i) a small number of $z \gtrsim 3$ Type 1 AGN, which are known to be excluded by the Paper I color selection; (ii) low-redshift, low-luminosity AGN with hosts bright enough to move their mid-IR colors below the WISE selection limit, but red enough to be picked by the Stern et al. (2005) IRAC selection criteria; and (iii) a higher incidence of contamination by $z \sim 0.5$ star-forming galaxies to the IRAC selection criterion which artificially lowers the completeness — though we note that this contamination is expected to be small at the depth of SDWFS (see Assef et al. 2010; Donley et al. 2012).

The cause of the significantly lower reliability obtained in the Boötes field compared to the COSMOS field is readily apparent in Figure 2. The modestly deeper WISE sample increases the number of contaminating galaxies, particularly to the left of the QSO locus. These correspond to high-redshift ($z \sim 1 - 1.5$) galaxies. The observed W2 magnitude of $z \sim 1 - 1.5$ L_* galaxies evolves very slowly with redshift (see, e.g., Fig. 1 of Eisenhardt et al. 2008), so there is a huge increase in contamination as soon as the W1 magnitude limit is deep enough to begin including these galaxies. In the Stern et al. (2005) IRAC selection criterion this problem is controlled using the [5.8]–[8.0] color, but the longer wavelength WISE bands are too shallow to help.

3.2. Magnitude-Dependent AGN Color-Selection

It is apparent from Figure 2 that an improved method to select AGN may be possible if we allow our color cut to evolve with magnitude since the major contaminants are either low-redshift, nearby star-forming galaxies which are intrinsically faint, or high-redshift, passive galaxies that are luminous enough to be bright in the WISE bands. In order to design a magnitude-dependent AGN color selection method that is applicable over the whole sky, we will go to fainter WISE fluxes than afforded by the 10σ W2 limit in the Boötes field. Note, however, that as we go to fainter W2 magnitudes, it becomes unreliable to use an AGN control sample based on the IRAC color criteria of Stern et al. (2005), as it is susceptible to contamination by high-redshift galaxies once the errors in the SDWFS IRAC [5.8] and [8.0] fluxes become too large (see, e.g., Donley et al. 2012). Instead, we define the control sample as all objects whose best-fit UV–mid-IR SEDs have a strong AGN component, as indicated by requiring $\hat{a} > 0.5$. For significantly lower levels of AGN activity, it becomes necessary to differentiate between objects where the AGN component of the fit is real and when it has only been used to mathematically improve the χ^2 to accommodate lower quality photometry

or mimic a galaxy component missing from the templates. This falls beyond the scope of the current work, and a full analysis on this topic is presented by Chung et al. (in prep.). Assef et al. (2010) has shown that the Stern et al. (2005) criterion is biased towards objects with large $\hat{a}$ values (see also §4.3), so we are not considerably changing the physical properties of the control sample by using this definition.

Figure 3 shows the completeness and reliability obtained as a function of W2 magnitude and the minimum W1–W2 color limit adopted to select AGN. We have required a minimum detection threshold of 3σ for W1 in order to have a reasonably precise WISE color. At bright W2, a color cut of 0.6 is sufficient to obtain high reliability and high completeness. Towards fainter W2 magnitudes, high reliability requires redder color cuts in order to remove contaminating galaxies, which also leads to lower completeness. The completeness of a color cut is relatively independent of W2 magnitude.

Figure 3 shows the bluest W1–W2 color at which 90% and 75% reliability is reached for a given W2 magnitude. While there is significant noise in these curves, they are reasonably well described by an exponential in W2[2]. Hence, we propose a WISE AGN color selection limit optimized for reliability given by

$$\mathrm{W1} - \mathrm{W2} > \alpha_{\mathrm{R}}\ \exp\left\{\beta_{\mathrm{R}}\ (\mathrm{W2} - \gamma_{\mathrm{R}})^2\right\}. \tag{3}$$

For W2<17.11, we achieve a reliability of ∼90% with $(\alpha_{R90}, \beta_{R90}, \gamma_{R90}) = (0.662, 0.232, 13.97)$. The corresponding values for a reliability of ∼75% are $(\alpha_{R75}, \beta_{R75}, \gamma_{R75}) = (0.530, 0.183, 13.76)$. The 90% (75%) reliability criterion reach our imposed W1 $S/N > 3$ limit at a W2 magnitude of 16.26 (16.45). Only considering objects brighter than this limit in W2, the 90% reliability criterion identifies 1174 AGN candidates, of which 1060 (90%) have their bolometric luminosities dominated by the AGN (e.g., $\hat{a} > 0.5$). For the 75% reliability criterion, we identify 2306 AGN candidates, of which 1752 (76%) are AGN-dominated. At a shallower depth of W2 <15.73, corresponding to $S/N > 10$ in the Boötes field, the 90% reliability curve identifies 1051 AGN candidates of which 950 (90%) are AGN-dominated, while the 75% reliability curve identifies 1582 AGN candidates of which 1200 (76%) are AGN-dominated. For comparison, a simple W1–W2≥0.8 cut (e.g., similar to the criterion of Paper I, but without its magnitude cut) finds 1746 AGN candidates with 74% reliability at a depth of W2 = 15.73. This census increases to 17997 AGN candidates to a depth of W2 = 17.11, albeit with a reliability that drops to 45%. These statistics are summarized in Tables 1 and 2. In the next section (§3.3) we compare this new magnitude-dependent AGN selection criterion to several other WISE AGN selection criteria that have recently been proposed in the literature.

Figure 3 also shows the reddest W1–W2 color at which 90% and 75% completeness is reached for objects with bolometric luminosities dominated by the AGN emission. In

this case, a reasonable description of the completeness boundary is given by the magnitude independent color cut

$$\mathrm{W1} - \mathrm{W2} > \delta_{\mathrm{C}}, \tag{4}$$

where $\delta_{C90} = 0.50$ for 90% completeness and $\delta_{C75} = 0.77$ for 75% completeness. Note that the 75% completeness criterion is basically equivalent to the cut proposed by Paper I, shown in equation 2, but without the flux cut. It is important to stress that these criteria are appropriate only for strong AGN with respect to their hosts due to the $\hat{a} > 0.5$ requirement.

While the magnitude dependence in the reliability-optimized criterion is caused in part by the much higher number of high redshift galaxies at fainter fluxes (see discussion in §3.1), it is also driven by the increasingly large errors in W1 and W2 at lower S/N. Since the S/N of WISE observations varies significantly across the sky, in principle α_R, β_R and γ_R may depend on ecliptic latitude. To test the strength of this dependence, we simulate the distribution of W1–W2 and W2 magnitudes for different WISE field depths and estimate α_R, β_R and γ_R in each case. For this we use the magnitudes obtained from the SED modeling of every object and we approximate that the S/N for a flux F depends on field depth as

$$\frac{S}{N} \;=\; K_1 \sqrt{\frac{N_F}{30}}\, \frac{F}{\sqrt{F + F_{\mathrm{Sky}}}}, \tag{5}$$

where N_F is the number of individual WISE 11s frames used to build the catalog image, K_1 is a constant and F_{Sky} is the background flux. This formulation neglects the effects of confusion as well as the variation of F_{Sky} with sky position is not uniform across the sky. However, our approximation should give a good general idea of how the parameters in question vary with N_F. As discussed earlier, $N_F^{\mathrm{Bootes}} = 30$, and we use the Boötes data to fit for K_1 and F_{Sky}. We find that from $N_F = 10$ to 50, no significant variation is observed for the α_{R} and γ_{R} parameters for both the 90% and 75% criteria. The parameter β_R is observed to decrease linearly by a factor of ~ 4 between $N_F = 8$ and $N_F = 25$, and is approximately independent of the depth of the field for $N_F \gtrsim 25$. Considering then a modified $\beta'_R = \beta_R^{\mathrm{Boo}}\,(5.41 - 0.176 N_F)$ may be necessary to achieve the proposed reliability levels in WISE fields with $N_F < 25$, where β_R^{Boo} is the value obtained for the Boötes field. We also repeat the experiment for the completeness optimized criteria, and find that in the same range of N_F, δ_C is approximately constant.

We refer to the reliability-optimized selection as R_{90} and R_{75} for 90% and 75% reliability, respectively, while C_{90} and C_{75} refer to the completeness-optimized criteria. Whether scientific interest lies in maximizing completeness or reliability depends on the problem at hand. However, it will be most common to wish to maximize reliability, so in the next sections we will focus on results for the highest reliability selection.

3.3. Comparison with the Literature

AGN identification using mid-IR broad-band photometry is now a well studied problem. The first classification schemes were developed for *Spitzer* IRAC and MIPS photometry (see, e.g., Lacy et al. 2004, 2007; Stern et al. 2005; Alonso-Herrero et al. 2006; Messias et al. 2012) and have been shown to be very successful in terms of both reliability and completeness. In the previous section we developed four AGN identification schemes using WISE W1 and W2 photometry, optimized to produce samples with different levels of either reliability or completeness. Several other WISE criteria have also recently been developed. Here we briefly discuss several of these criteria and discuss how they compare to our selection criteria. This is meant to be an illustrative rather than an exhaustive exercise; we do not discuss all the published mid-IR selection techniques.

Tables 1, 2 and 3 show the surface density of AGN candidates, their reliability and their completeness for the selection criteria of §3.2, Paper I, Jarrett et al. (2011), Mateos et al. (2012) and Wu et al. (2012b). Table 1 restricts the samples to W2<17.11 (W2 $S/N > 3$ in Boötes), while Table 2 uses the more restrictive flux cut of W2<15.73 (W2 $S/N > 10$ in Boötes). The samples used in all tables are also restricted to W1<18.50, but no restriction is applied in W3 and W4. For completeness, Table 3 further limits the sample to W2<15.05 (W2 $S/N > 10$ in COSMOS), which is representative of the shallowest WISE observations, but we will not discuss it in detail. We also include the selection criteria proposed by Assef et al. (2010), which was obtained by simulating WISE photometry using SED models of all objects in SDWFS. For comparison, we also show the numbers for the IRAC-based selection criteria of Lacy et al. (2004, 2007), Stern et al. (2005) and Messias et al. (2012), calculated using the SDWFS photometry. As was done in the previous section, reliability and completeness are measured against the number of objects whose SED fits have $\hat{a} > 0.5$.

For the WISE selection methods, regardless of the W2 depth, the most reliable sample is that based on the W1, W2, W3 and W4 selection criteria of Assef et al. (2010), with a 97% and 98% reliability for W2<17.11 and W2<15.73, respectively. However, because it requires that W4 is detected, it also has the lowest completeness (9% and 19% for W2<17.11 and W2<15.73, respectively) as measured by the surface density of AGN candidates, with only 43 deg^{-2} candidates with W2<17.11. Our R_{90} is the second most reliable criterion, with 90% reliability by design, but it has a much higher completeness, with 53% for W2<15.73 and 9% for W2< 17.11, which translates into AGN candidate surfaces densities of 117 and 130 deg^{-2} respectively . The four-band criterion of Mateos et al. (2012) also has high reliability, although it is below our R_{90} criterion in both reliability and completeness. Both of the W1, W2 and W3 based selection criteria of Jarrett et al. (2011) and Mateos et al. (2012) are similar in reliability and completeness, comparable to our R_{75} criterion for W2<15.73,

but somewhat less reliable for W2<17.11. As discussed by Jarrett et al. (2011), the strength of these criteria are in the deepest WISE fields, where W1 and W2 depths are below the confusion limit.

With respect to the IRAC-based criteria, the most reliable of those shown is that of Stern et al. (2005), which is expected based on the discussion of Assef et al. (2010). In terms of completeness levels, we note that all criteria shown are similar, except for the "KI" criteria of Messias et al. (2012) based on K_s, [4.5] and [8.0] photometry, which has a significantly higher completeness of about 90%, although with poor reliability. It is also important to notice that, in principle, completeness and reliability could be improved by further adding more information based on other wavelength regimes. Such is the case, for example, with the "S_{IX}" selection scheme of Edelson & Malkan (2012), which combines WISE, 2MASS and ROSAT data to identify the brightest AGN in sky. Including this kind of selection is, however, beyond the scope of this comparison.

4. Properties of WISE AGN Candidates

In this section we study the properties of the WISE AGN candidates selected using the criteria developed in the previous section. We first discuss the accuracy to which we can determine photometric redshifts for them. In §4.2 we discuss their redshift distribution, and in §4.3 we discuss the parameters derived from our SED fitting. In §4.4 we present spectroscopic observations of a sample of photometrically selected high redshift Type 2 AGN candidates.

4.1. Photometric Redshift Accuracy for WISE AGN Candidates

Several authors (e.g., Brodwin et al. 2006; Rowan-Robinson et al. 2008; Salvato et al. 2009; Assef et al. 2010) have shown that photometric redshifts of Type 1 AGN are relatively inaccurate when relying solely on broad-band photometry, as is our case. This is mostly due to the lack of strong spectral features that are necessary for anchoring the photometric redshift estimates. Our AGN sample is, however, brighter than those typically studied for photometric redshifts, and has a considerable number of Type 2 AGN. Photometric redshifts for Type 2 AGN may be better because the spectral features of the host galaxy are relatively stronger.

We estimate photometric redshifts as discussed in §2.3, using, in addition to WISE, all the UV through mid-IR broad-band photometry of the field described in §2.1. As in

Assef et al. (2010), we quantify the photometric redshift accuracy using the statistic

$$\Delta z \;=\; \left[\frac{1}{N}\sum_i \left(\frac{z^i_{\rm phot}-z^i_{\rm spec}}{1+z^i_{\rm spec}}\right)^2\right]^{1/2}, \tag{6}$$

where the index i sums over all objects in a sample and N is their total number. This estimate of the dispersion, however, is typically driven by outliers, so we also estimate Δz_{95}, the dispersion calculated including only the 95% of objects with the best photometric redshift estimates.

Panel a) of Figure 4 shows the spectroscopic and photometric redshifts obtained for the full W2 depth R_{90} AGN candidates, limited to objects with $\hat{a} > 0.5$ to be certain we only study the objects of interest. Table 4 shows the dispersion as well as the median offsets for the remaining criteria, again limited to $\hat{a} > 0.5$. It also shows the number of AGN used to compute the statistic and the fraction of objects in every selection criteria that have spectroscopic redshifts. Irrespective of the selection method, the photometric redshifts are fairly inaccurate, with $\Delta z_{95} = 0.20 - 0.23$ ($\Delta z = 0.27 - 0.31$). This is consistent with the results presented by Assef et al. (2010) for a similar, but fainter, sample of objects. The pile-up of objects at very low $z_{\rm phot}$ is a degeneracy caused by the galaxy luminosity prior. However, these are only a small part of the sample, and eliminating the prior results in even less accurate estimates for the general population. Panel b) shows that little is gained in terms of the accuracy when limiting the sample to the brighter W2 $S/N > 10$ objects. The same is observed when the sample is further limited by requiring $I < 20$, as shown in Panel c).

If we further split the bright, final sample (W2 < 15.73 and $I < 20$) and only investigate objects with considerable obscuration, $E(B-V) > 0.5$, we find that Δz_{95} drops by $\sim 45\%$, although Δz either decreases only slightly (R_{90} and C_{75}), or increases (R_{75} and C_{90}). That these accuracies are still much worse than the $\Delta z_{95} \sim 0.04$ found by Assef et al. (2010) for galaxies of equivalent brightness is most likely due to the sample requirement that $\hat{a} > 0.5$, meaning that even though reddened, the accretion disk emission is still likely dominant, or at least significant, in many of the broad-bands used.

As mentioned earlier, Assef et al. (2010) showed that although photometric redshifts for AGN based on broad-bands can be inaccurate, the value of $\hat{a}$ obtained from the corresponding SED fit is insensitive to the redshift accuracy, i.e., that $\hat{a}$ is relatively independent of photometric redshift. As one of our goals is to study the obscuration in AGN in a statistically significant manner, we can ask if this holds for the inferred reddening of the AGN component. Unfortunately this is not the case; while objects with good photometric redshift estimates have consistent estimates of $E(B-V)$, objects where $z_{\rm phot}$ is considerably in error

have inaccurate and typically underestimated values of $E(B-V)$. This will be of particular importance in §5.

4.2. Redshift Distribution of WISE AGN Candidates

Using the cuts developed in the previous section we now study the redshift distribution of the different samples of AGN candidates. Although we have a large amount of spectroscopic observations in the Boötes field, we are still missing spectroscopic redshifts for a considerable number of our AGN candidates (see Table 4 for details). For the objects without spectroscopic redshifts, we use the photometric redshift estimates detailed in §2.3, although these may not be very accurate (see §4.1). We focus on the R_{90} sample, which mitigates this issue as these objects are the ones most likely to have spectra from the AGES survey (see §2.1 and Kochanek et al. 2012, for details).

Figure 5 shows the redshift distribution of the W2, W1 $S/N > 3$ depth R_{90} sample. The resulting distribution of AGN is double peaked, with the main peak at $1 \lesssim z \lesssim 2$ and a smaller peak at $z \sim 0.25$. Almost no objects are at $z \gtrsim 3$. This distribution reflects that WISE has a high sensitivity to obscured AGN at lower redshifts, where the AGN emission still dominates the observed W1 and W2 fluxes. However, as the redshift increases or the galaxy host contributions become larger, the bias against obscured sources increases. This causes the minimum at $z \sim 0.75$, followed by an increase simply from the increase in comoving volume probed. The W1–W2 color of Type 1 AGN is reddest at $1 \lesssim z \lesssim 2$ (see Fig. 1), and progressively gets bluer at higher redshift, falling completely out of the selection criteria by $z \sim 3$. A similar behavior is observed for the R_{75}, C_{75} and C_{90} samples, although since contaminants appear preferentially at high redshifts (see §3.2), the balance between the peaks for the complete $\hat{a}$ samples is modified. Figure 5 shows that a large number of the R_{90} AGN candidates (56%) have spectroscopic redshifts. Furthermore, objects lacking spectroscopic redshifts tend to follow a similar redshift distribution, implying that although the uncertainties in the photometric redshifts are very large, they do not seem to systematically bias the distribution. Limiting the samples to only the brighter W2 $S/N > 10$ objects does not significantly change the shape of the redshift distribution.

4.3. SED Analysis of WISE AGN Candidates

A simple way of quantifying the contamination rates in the criteria we have defined is by looking at the best-fit combination of SED templates to their photometry. The most relevant

parameter is $\hat{a}$, defined in equation (1). As mentioned earlier, this parameter has the useful property of being relatively insensitive to photometric redshift uncertainties (see Assef et al. 2010, for details). Figure 6 shows the distribution of $\hat{a}$ for our full-depth R_{90} and C_{90} AGN candidate samples. We find that the R_{90} sample is skewed towards objects dominated by their AGN component, with almost no objects being best-fit as inactive galaxies. This feature is also observed, although to a somewhat lesser degree, in the R_{75} sample. The C_{90} sample, on the other hand, shows a very considerable peak at $\hat{a} = 0$, as expected given its low reliability but high completeness. It also shows, however, a very significant increase in the number of objects with intermediate $\hat{a}$ values. These dominate the distribution for $\hat{a} > 0$. Most such objects probably correspond to real AGN with high host fractions, implying that our reliability optimized criteria is strongly biased against such objects.

It is well known that the luminosity of the spheroidal component of the host galaxy is correlated with the mass of its central SMBH, and that this relation is roughly linear: $L_{\rm host} \sim M_{\rm BH}$ (see, e.g., Magorrian et al. 1998; Ferrarese & Ford 2005; Graham 2007, although also see Graham 2012 for possible deviations). Some authors have postulated that the correlation is also present, and non-evolving, when considering the total host galaxy luminosity instead of just the spheroidal component (Bennert et al. 2010). Regardless, since the Eddington luminosity $L_{\rm Edd}$ is directly proportional to $M_{\rm BH}$, the Eddington ratio $\ell_{\rm Edd}$ can be expressed as

$$\ell_{\rm Edd} \;=\; \frac{L_{\rm AGN}}{L_{\rm Edd}} \;\sim\; \frac{L_{\rm AGN}}{L_{\rm Host}} \;=\; \frac{\hat{a}}{1-\hat{a}}. \tag{7}$$

Hence, to first order, AGN whose bolometric output is dominated by the AGN emission (i.e., have high $\hat{a}$ values) also correspond to objects emitting at a high $\ell_{\rm Edd}$. Similarly, those galaxies for which stellar light represents a higher fraction of their total bolometric output (i.e. low $\hat{a}$) are likely radiating at lower Eddington ratios. So, in a physical context, we see that our reliability-optimized selection criterion is strongly biased against AGN radiating at low $\ell_{\rm Edd}$, but as our selection criterion is shifted to emphasize high completeness, we start recovering them.

Figure 6 also shows the distribution of $\hat{a}$ limited to W2 < 15.73. While the R_{90} sample looks nearly the same, the C_{90} sample exhibits a different distribution, with the contamination ($\hat{a} = 0$ peak) and the skewness of the distribution shifting to be more similar to the R_{90} sample. Partly, this is because the largest contamination in completeness-optimized samples comes from high-redshift galaxies, which are avoided by the R_{90} criterion. That the peak at high $\hat{a}$ is increased is possibly due to low Eddington ratio AGN simply being less luminous on average.

The other SED-fit parameter of interest is the amount of obscuration towards the AGN, which is shown in Figure 7 for the R_{90} AGN sample at full and 10σ W2 depths. The most

important result to notice is that the WISE AGN selection is sensitive even to objects with high obscuration. In order to interpret the distribution, however, we need to deal with two issues. The first is that because of the algorithm design, the reddening may be slightly underestimated. Second, we need to take into account the selection function of AGES, since the reddening obtained from objects with only photometric redshifts estimates can be inaccurate (§4.1). We deal with both issues and present a detailed study of the reddening properties of AGN in Section 5.

4.4. Keck Observations

To highlight the power of WISE in finding highly obscured quasars, we obtained additional spectroscopy of 12 AGN candidates at the Keck Observatory in April 2011. Since the AGES spectroscopy is limited to $I < 22.5$, and is highly complete for $I < 21.5$, we emphasized optically fainter candidates which are bright in W2, selected on the basis of an early version of the Paper I criteria. We furthermore required them to not have a measured redshift. Because these observations used a preliminary version of the WISE data, some of the WISE colors and positions changed relative to the more accurate all-sky release. Therefore, the sources we observed have a range of WISE colors and optical magnitudes; based on the WISE all-sky data release, all but one of them are sufficiently red in W1−W2 to be classified as AGN candidates by at least the C_{90} criterion, but not all of them are optically faint ($I > 21$). However, most of the targets do meet the R_{90} selection criterion and prove to be *bona fide* obscured quasars (see Table 5 for W1–W2 color, W2 magnitude and AGN classification criteria met by each target).

We observed three Keck slitmasks in the Boötes field with the DEep Imaging Multi-Object Spectrograph (DEIMOS; Faber et al. 2003) on UT 2011 April 1-3. We used the 4000 Å order-blocking filter and the 600 ℓ mm^{-1} grating (blazed at 7500 Å; resolving power $R \equiv \lambda/\Delta\lambda \sim 1600$ for the 1.″2 wide slitlets we employed). We observed a single additional mask using the dual-beam Low Resolution Imaging Spectrometer (LRIS; Oke et al. 1995) on UT 2011 April 28. The LRIS observations employed the 300 ℓ mm^{-1} grism on the blue arm of the spectrograph (blazed at 5000 Å; $R \sim 500$), the 400 ℓ mm^{-1} grating on the red arm of the spectrograph (blazed at 8500 Å; $R \sim 700$), and 6800 Å dichroic. Data reduction followed standard procedures, and we flux calibrated the data using standard stars from Massey & Gronwall (1990).

Table 5 summarizes the results for these observations, including measured redshifts, selection criteria, and the best-fit $\hat{a}$ and AGN reddening parameters for the adopted redshift, with errors derived from Monte Carlo re-sampling of the data. The Appendix presents

the results for additional Boötes targets observed on these masks. We include the quality ("Q") of each spectroscopic redshift. Quality flag "A" signifies an unambiguous redshift determination, typically relying upon multiple emission or absorption features. Quality flag "B" signifies a less certain redshift determination, such as the robust detection of an isolated emission line, but where the identification of the line is uncertain (e.g., Stern et al. 2000). Quality flag "B" might also be assigned to a source with a robust redshift identification, but where some uncertainty remains as to the astrometric identity of that spectroscopic source. We consider the quality "B" results likely to be correct, but additional spectroscopy would be beneficial.

Figure 8 shows the best-fitted SEDs for each of the 8 targets, from the original 12, whose all-sky release WISE W1−W2 colors classify them as AGN by either the R_{90} or R_{75} criterion. Upon inspecting the optical images, we believe the bright, discrepant I-band flux of W1430+3530 is most likely due to a bright star within $30''$ contaminating the photometry. Although most of these objects appear to be real AGN based on their broad-band SEDs, many lack strong, high-ionization lines such as C IV, Mg II and Ne V, even though lower ionization lines common for star-formation are indeed observed (see Table 5). The X-ray community has noticed a related population of X-ray bright, optically normal galaxies (XBONGs; e.g., Civano et al. 2007) where the X-ray luminosities require the presence of an actively accreting SMBH while optical spectroscopy reveals an apparently normal, inactive galaxy. Several explanations have been offered to explain such sources, ranging from systematic effects that dilute the AGN signature for the wide slit widths typically used for these distant sources (e.g., Moran et al. 2002), to radiatively inefficient accretion flows (e.g., Trump et al. 2011). Alternatively, at least some of these objects could be better described as AGN dominated LIRGs or ULIRGs, where the lack of high ionization emission lines and the red host color may be explained by large scale obscuration. Some evidence of the Si 9.7μm absorption feature typical of ULIRGs may be present in a few cases (W1427+3408, W1431+3525, W1432+3523 and W1432+3526), although this feature may also be observed in AGN under certain conditions (see, e.g., Feltre et al. 2012).

5. Dust Reddening in AGN

In this section we study dust obscuration properties of a set of 362 $z < 1$ AGN well detected by WISE with spectroscopic redshifts, $I < 20$ and $\hat{a} > 0.5$ in the Boötes field. As argued earlier, low redshift ($z \lesssim 1$) WISE AGN selection criteria are relatively insensitive to obscuration since they rely on the hot dust emission from the dust torus instead of on the blue colors of the unobscured accretion disk emission, as per optical selection. Hence, we

can use WISE to study the properties of dust obscuration in AGN.

AGN unification models (see, e.g., Antonucci 1993; Urry & Padovani 1995) propose that Type 1 and Type 2 AGN are physically equal but are observed at different inclination angles relative to the obscuring material near the AGN. Typically it is assumed that the accretion disk, responsible for the $\lambda \lesssim 1\mu$m continuum emission, extends to radial scales of ~ 10 AU, and is surrounded by highly ionized gas responsible for the broad emission-lines. On larger scales (~ 1 pc) there is dust in the general shape of a "torus" or a flared disk, responsible for the Type 1/Type 2 dichotomy, that absorbs the optical radiation from the accretion disk and re-emits it in the mid-IR. We refer to this structure as the torus, as is commonly done, although we do not *a priori* assume a shape for it. The inner edge of the dust torus is determined by where the dust reaches its sublimation temperature due to heating from the accretion disk. Such hot dust produces the emission observed to dominate the mid-IR portion of the AGN SED. Furthermore, narrow emission lines are observed in both Type 1 and Type 2 AGN, and are known not to be polarized (e.g., Antonucci 1993), so the dust structure must be smaller than the narrow line region (~ 1 kpc). Given that the Type 1/Type 2 dichotomy is also manifested in the neutral hydrogen absorption of the X-ray emission, the torus must also be associated with the absorbing gas.

Many properties of the dust torus have been extensively studied. For example, several authors (e.g., Krolik & Begelman 1988; Nenkova et al. 2002, 2008; Elitzur & Shlosman 2006; Tristram et al. 2007) have argued that the dust in the torus must be in optically and geometrically thick clumps to reproduce observations, while others (e.g., Dullemond & van Bemmel 2005; Fritz et al. 2006) argue the dust may be smoothly distributed. A recent study by Feltre et al. (2012), however, suggests that given the same dust composition and the same illuminating source, the difference in the broad-band shape of the SEDs from these dust configurations may be too subtle to distinguish between both scenarios with current data. In a more global sense, the geometry and evolution of the obscuring structures have also been studied, as, for example, the fraction of obscured objects can have profound implications over explaining the cosmic hard X-ray background (see, e.g, Ueda et al. 2003). Simpson (2005) has shown using the Type 1 and Type 2 AGN optical luminosity function from SDSS that the fraction of Type 2 AGN increases with decreasing accretion disk luminosity, and a similar behavior has been observed for radio galaxies (Lawrence 1991; Simpson 1998; Grimes et al. 2004) and in the X-rays (e.g., Ueda et al. 2003; Hasinger 2004). Such a behavior can be naturally expected if the scale height h of the obscuring material is independent (or not linearly related) to the radial size of the structure ($R \propto \sqrt{L_{\rm AGN}}$), such that for brighter AGN the dust effectively covers a smaller solid angle as viewed from the SMBH. This scenario is usually referred to as the "receding torus model", and was first proposed by Lawrence (1991). In particular, Simpson (2005) has shown that observations appear to be best reproduced if

$h \propto L_{AGN}^{0.23}$.

Combining WISE and all the ancillary observations in the NDWFS Boötes field and performing the SED modeling as detailed in §2.3, we can study the average properties of dust obscuration in AGN by counting the number of objects observed per unit reddening. This approach allows us to quantify the fraction of AGN that can be classified as Type 1, and also, in principle, to differentiate between different dust geometries and compositions. Note that obscuring dust may also be present in the interstellar medium (ISM) of the respective host galaxies, and while we expect AGN obscuration to be mainly driven by the dust in the torus and hence delineate the discussion in that direction, we further address galactic-scale obscuration in §5.3. Since our sample is, in essence, flux limited, our analysis must properly take into account its selection function. Specifically, it must account for all the biases against highly obscured objects, since higher AGN obscuration can also make the objects appear much fainter depending on the relative contribution and SED shape of the host galaxy. Fortunately, the SED fitting approach of Assef et al. (2010, see also §2.3) is well suited to assess and correct for our survey incompleteness. In the next section we detail our sample selection function. In §5.2 we detail the formalism we use to incorporate the selection function in our measurement of the reddening distribution, while in §5.3 we show and discuss the resulting distributions.

5.1. Sample Selection Function

To study the reddening distribution, we use a subsample of the larger sample described in §2. We require that objects have W2 < 15.73, a measured spectroscopic redshift such that $E(B-V)$ is accurately estimated (see §4.1), and $\hat{a} > 0.5$ to minimize possible non-AGN contaminants. Note that we do the initial selection with the SED fits obtained including all the priors described in §2.3, which is necessary to ensure all obscured AGN are real. As discussed there, this can lead to slightly underestimated AGN obscuration. Hence, once the sample is selected, we re-fit the SEDs removing all priors described in §5.3 to obtain the final $E(B-V)$ values, although we note not removing the prior does not qualitatively affect our results. We visually inspected the SED fit of every source and eliminated 16 galaxies where we believed the AGN classification or the reddening values were spurious due to bad photometry.

We further require that the redshift was determined by AGES, since its well determined selection function is a crucial component of our analysis. Since many of the objects we consider are extended in the NDWFS imaging and were not necessarily targeted as AGN candidates by the AGES survey, we must also restrict our sample to objects with $I < 20$,

resulting in a final sample size of 362 AGN. AGES was designed to ensure subsamples are statistically complete to $I < 20$ for galaxies and $I < 21.5$ for AGN (see Kochanek et al. 2012, for details). In order to do this, AGES used a sparse sampling algorithm for galaxies, such that for every defined galaxy subsample, a spectrum was attempted for all objects brighter than a certain magnitude limit and for a percentage (typically 20–30%) of randomly selected fainter galaxies down to a certain magnitude. For example, the main I-band selected galaxy sample was observed in full for $I < 18.5$ and 20% of the galaxies were followed in the range $18.5 < I < 20$. In contrast, there was no sparse sampling for AGN candidates as AGES attempted to get spectra of all of them. Every subsample was assigned a selection code, where $P^n_{i,\mathrm{sparse}}$ is the probability that object i of the subsample with selection code n was selected for spectroscopy due to the sparse sampling algorithm.

In addition, the fraction of sources with a successfully measured redshift depends on I-band magnitude. While the survey design minimized the magnitude dependence beyond the sparse sampling, there is still a dependency simply because it is more difficult to obtain redshifts for fainter sources in a fixed integration time. Using the full results of the AGES survey, we estimate for every selection code the fraction of objects for which spectra were attempted and a redshift was measured as a function of I-band magnitude, $P^n_{i,I}$.

In order to correct for the selection function, we need to estimate for every object the probability that objects with the same optical and IR magnitudes would have been observed, so that we can statistically account for those without spectroscopic observations. Since every object may have been targeted for more than one of the different subsamples, we need to consider the joint probability of all subsamples. Let $P^n_i = P^n_{i,\mathrm{sparse}} \times P^n_{i,I}$ and let N be the total number of subsamples object i is part of. We define $C(N,k)$ to be the sum of all possible combinations of k element products of the P^n_i terms, such that, for example, $C(3,1) = P^1_i + P^2_i + P^3_i$, $C(3,2) = P^1_i P^2_i + P^1_i P^3_i + P^2_i P^3_i$ and so on. The probability a spectroscopic redshift would have been obtained for objects like object i is then given by

$$P_i \;=\; \sum_{k=1}^{N} (-1)^{k+1}\, C(N,k). \tag{8}$$

It can be shown that if any of the terms $P^n_i = 1$, then $P_i = 1$, as would be expected. For consistency with the original AGES selection, we use the original catalogs of AGES to assess the spectroscopic completeness rather than the catalogs described in §2.

5.2. Method

In order to incorporate the selection function, we adapt the step-wise maximum likelihood method (SWML) of Efstathiou et al. (1988). For the remainder of this section, we define $E_{BV} \equiv E(B-V)$. Our goal is to estimate the distribution $\xi(E_{BV}) = dn/dE_{BV}$, where we remind the reader that E_{BV} corresponds to the reddening only over the AGN component, not over the host galaxy (see §2.3 for details). The probability of finding an object with a given reddening E^i_{BV} is given by

$$p_i \;\propto\; \left(\frac{\xi(E^i_{BV})}{\int_0^{E^i_{BV,\mathrm{Max}}} \xi(E_{BV}) dE_{BV}} \right)^{C_i}, \tag{9}$$

where $C_i = P_i^{-1}$ is calculated using equation (8) and $E^i_{BV,\mathrm{Max}}$ is the maximum reddening object i could have and still be in our sample, which we detail below. We estimate $E_{BV,\mathrm{Max}}$ by varying the reddening of the AGN component of the best-fit combination of SED templates but keeping the amplitude of the components fixed (see §2.3 for details).

To apply the SWML method we discretize the function $\xi(E_{BV})$ in bins of E_{BV} rather than assuming a parametric form. We divide $\xi(E_{BV})$ into N_p bins of value ξ_k, centered at reddening values ϵ_k with widths ΔE_{BV}. We can then rewrite equation (9) as

$$p_i \;\propto\; \left(\frac{\sum_{k=1}^{N_p} W(E^i_{BV} - \epsilon_k)\; \xi_k}{\sum_{j=1}^{N_p}\; H(\epsilon_j - E^i_{BV,\mathrm{Max}})\; \xi_j\; \Delta E_{BV}} \right)^{C_i}, \tag{10}$$

where

$$W(x) \;=\; \begin{cases} 1 & \text{if } -\Delta E_{BV}/2 \le x \le \Delta E_{BV}/2, \\ 0 & \text{otherwise} \end{cases} \tag{11}$$

and

$$H(x) \;=\; \begin{cases} 1 & \text{if } x < -\Delta E_{BV}/2, \\ \frac{1}{2} - \frac{x}{\Delta E_{BV}} & \text{if } -\Delta E_{BV}/2 \le x \le \Delta E_{BV}/2, \\ 0 & \text{if } x > \Delta E_{BV}/2. \end{cases} \tag{12}$$

The likelihood $\mathcal{L}$ of our sample being drawn from the distribution $\xi(E_{BV})$ corresponds to the multiplication of the p_i values of all N_{AGN} objects in our sample. Taking the gradient of $\mathcal{L}$ with respect to $\vec{\xi} = (\xi_1, \ldots, \xi_k)$, we can find that the values that maximize the likelihood are given by

$$\xi_k \Delta E_{BV} \;=\; \frac{\sum_{i=1}^{N_{\mathrm{AGN}}}\; C_i\; W(E^i_{BV} - \epsilon_k)}{\sum_{i=1}^{N_{\mathrm{AGN}}}\; \frac{C_i\; H(\epsilon_k - E^i_{BV,\mathrm{Max}})}{\sum_{j=1}^{N_p}\; H(\epsilon_j - E^i_{BV,\mathrm{Max}})\; \xi_j\; \Delta E_{BV}}}. \tag{13}$$

As discussed by Efstathiou et al. (1988), a constraint is needed since the likelihood only depends on the ratios of the ξ_k values. We adopt the constraint

$$g(\vec{\xi}) = \sum_{k=1}^{N_p} \xi_k - N_{\rm AGN}, \tag{14}$$

so that the sum of the bins simply equals the number of AGN, and we maximize $\ln \mathcal{L}' = \ln \mathcal{L} + \lambda g(\vec{\xi})$, where λ is a Lagrange multiplier. Errors in ξ_k are estimated using the information matrix as detailed in Efstathiou et al. (1988). In practice, since most of our objects have relatively low reddening values, we prefer to estimate $\xi'(E_{BV}) \equiv dn/d\log(E_{BV}+0.1)$. Finally, as discussed by Assef et al. (2011), our AGN SED template is as blue as possible, so some of the reddening we find is possibly just due to intrinsic differences in the SEDs of Type 1 AGN. For example, the mean Type 1 SED template of Richards et al. (2006) is similar to our AGN template with $E(B-V) \approx 0.05$. Since we do not want this to bias the results, we subtract 0.05 from all the $E(B-V)$ values before we construct $\vec{\xi}$.

5.3. Results

Figure 9 shows the distribution of $\xi'(E_{BV})$ derived using the sample described in §5.1. The key thing to note is that the distribution falls with increasing reddening, with a dip at $E(B-V) \sim 2$. A smaller, less significant dip may also be present at $E(B-V) \sim 0.15$. Note that there are no objects observed with a best-fit $E(B-V) > 14$. Luminous objects with such high reddening are expected to be rare (see, e.g., Eisenhardt et al. 2012; Wu et al. 2012a; Bridge et al. 2012, for such extreme cases). While the general trend of decreasing numbers with increasing reddening is in all likeliness real, our sample is small enough that the observed dips could in principle be systematic and caused by the non-parametric method we used, as it never imposes the requirement of a smooth distribution. However, when the sample is divided into three luminosity bins with equal numbers of objects, as shown also in Figure 9, the minimum of the dust distribution at $E(B-V) \sim 2$ appears in all of them, further suggesting this feature is real. Assuming that is the case, a few possible explanations are possible.

In the simplest orientation models for AGN unification, most of the obscuration comes from the dust torus. However, if the minimum at intermediate $E(B-V)$ is real, it is unlikely that the dust forms a continuous medium, as it is very hard to have a physically motivated dust distribution that produces such a feature. If the dust is, on the other hand, in geometrically and optically thick clouds, the distribution would simply be the distribution of the obscuration of the clouds convolved with the distribution of inclination angles and

covering fractions. However, this is also unlikely to be consistent with a minimum in the distribution at an intermediate obscuration value. Possibly, thick dust clouds are responsible for the $E(B-V) \gtrsim 2$ obscuration, and these are embedded in a diffuse inter-cloud dust medium which is responsible for the lower obscuration part of the $\xi'(E_{BV})$ distribution.

Alternatively, the two halves of the distribution could be attributed to different sources, with the large obscuration coming from thick dust clouds in a torus-like structure surrounding the AGN, and the lower obscuration coming from diffuse dust in the host galaxy ISM. Naively, one would not expect the distribution of ISM dust obscuration to vary systematically with AGN luminosity. When we divide the sample in three bins of luminosity with equal numbers of objects, as shown in Figure 9, we observe a significantly different shape for the $\xi'(E_{BV})$ distribution in each bin. We consider this as evidence that the dust obscuration is primarily coming from the vicinity of the AGN and is hence associated with the torus, and we discuss this below in the context of a receding torus. It may be possible that in certain AGN feedback scenarios the column density of the residual dust in the ISM left after the AGN has gone through the blow-out phase (see, e.g., Hopkins et al. 2008) could be related to AGN luminosity during its quasar phase.

Note that since our sample is inherently magnitude limited, we cannot easily disentangle redshift evolution from luminosity evolution. We consider, however, that it is much more likely that the evolution in the dust obscuration is primarily driven by the AGN luminosity since hardly any evolution is observed in the UV through mid-IR SEDs of AGN with cosmic time (e.g., Richards et al. 2006; Assef et al. 2010). Furthermore, Ueda et al. (2003) has shown that the distribution of neutral gas column densities obscuring the X-ray emission of AGN is independent of redshift.

We also investigate the fraction of Type 1 to Type 2 AGN by simply adding up the corresponding bins of the $\xi'(E_{BV})$ distribution. We adopt the standard X-ray boundary of a gas column density of $N_H = 10^{22}$ cm^{-2} (e.g., Ueda et al. 2003) as the dividing line. Maiolino et al. (2001) has shown that the value of $E(B-V)/N_H$ is significantly below the Galactic value for AGN, and varies significantly among different AGN. The median value of the Maiolino et al. (2001) sample is $E(B-V)/N_H = 1.5 \times 10^{-23}$ cm^2 mag, which puts the Type 1/2 boundary at $E(B-V) = 0.15$, or $A_V = 0.47$ for $R_V = 3.1$. It also implies that our sample does not contain any Compton-thick AGN ($N_H > 10^{24}$ cm^{-2}). From the joint distribution of all AGN, we find that the fraction of objects that would appear as Type 1 AGN is $47 \pm 8\%$, consistent with an even split between the two types. From a purely observational point of view, this is only strictly appropriate for $I < 20$ AGN given our sample selection. However, we note that very little variation in this ratio with $I-$band magnitude is observed in our sample.

Figure 10 shows the fraction of Type 1 AGN as a function of luminosity when we divide the sample into three luminosity bins with equal numbers of objects per bin. There is a sharp increase in the Type 1 fraction towards higher luminosities. For the lowest luminosity bin we find that the fraction of objects appearing as Type 1 is $29 \pm 7\%$, increasing to $46 \pm 15\%$ for the intermediate luminosity bin, and to $64 \pm 13\%$ at the highest luminosity. This trend conforms to the idea of a receding torus. Figure 10 compares our observed trends with three different models of a receding torus, taken from Simpson (2005). We model the fraction of Type 1 AGN by

$$f_1 \;=\; 1 \;-\; \left[1 \;+\; 3\left(\frac{L_{\rm AGN}}{L_{\rm AGN,0}}\right)^{1-2\psi}\right]^{-0.5}, \tag{15}$$

which comes from the simple geometry assumed by Simpson (1998) and assuming the scale height $h \propto L_{\rm AGN}^{\psi}$. At luminosity $L_{\rm AGN,0}$, AGN are evenly split between Types 1 and 2. We first consider the two cases studied by Simpson (2005), namely that of a constant h ($\psi = 0$), and his favored scenario of $\psi = 0.23$. Note that because Simpson (2005) used [O III] luminosities as proxies for the accretion disk luminosity, we must fit for $L_{\rm AGN,0}$, obtaining respectively $1.12^{+0.16}_{-0.14} \times 10^{45}$ erg s^{-1} ($\psi = 0$) and $1.98^{+0.57}_{-0.44} \times 10^{45}$ erg s^{-1} ($\psi = 0.23$). As shown in Figure 10, both of them give a fair representation of the data. If we also fit for the dependence of h on $L_{\rm AGN}$, we find $\psi = 0.13 \pm 0.17$ and $L_{\rm AGN,0} = 1.42^{+10.9}_{-1.26} \times 10^{45}$ erg s^{-1}. Unfortunately, our modest sample size does not allow us to more finely sample the Type 1 AGN fraction as a function of AGN luminosity and thereby further constrain such models. We do note, however, that the reddening distributions shown in Figure 9 have significant power to further constrain the dust distribution. This will be be further explored in future work.

6. Conclusions

In an earlier study (Paper I) we used the extensive spectroscopy and photometry of the 2 deg^2 COSMOS field to study WISE AGN selection. We found that the simple criterion W1–W2$\geq$0.8 and W2$<$15.05 produces a sample with 95% reliability and recovered 78% of the AGN found with *Spitzer* IRAC imaging to the same flux depth. Here we have extended this study using the larger 9 deg^2 NDWFS Boötes field, which has also significantly deeper WISE observations than COSMOS. We show that the reliability of a simple color cut quickly degrades towards fainter fluxes due to the large number of $z \gtrsim 1$ galaxies that contaminate the color selection.

Using the extensive UV through mid-IR broad-band photometry available in the NDWFS Boötes field we have studied W2–dependent W1–W2 selection criteria optimized to

find AGN at deeper WISE fluxes than those available in the COSMOS field. We provide different criteria depending on whether the emphasis is on reliability or completeness. We defined a reliability-optimized criteria as a W1–W2 color limit that varies as an exponential of $W2^2$, where the parameters can be tuned to achieve different reliability levels (§3.2). We find that for completeness-optimized selection, no dependence on W2 is needed; a simple W1–W2 color criterion suffices. We find that the criterion of Paper I returns samples with a completeness of approximately 75%.

We have also studied the accuracy of broad-band photometric redshifts obtained for the WISE AGN candidates using the Assef et al. (2010) basis of low-resolution SED templates for AGN and galaxies. We find consistency with the poor accuracy found by previous studies, even though our AGN are brighter than those typically used in such studies. Furthermore, we find that although the value of the $\hat{a}$ parameter, the luminosity fraction of the AGN with respect to the host plus the AGN, is insensitive to uncertainties in the photometric redshift, the best-fit reddening of the AGN component is strongly affected by those uncertainties. We have studied the distribution of the best-fit $\hat{a}$ parameter of the WISE AGN candidates, showing they are biased towards high values. This means that WISE AGN selection is biased towards objects that are bright with respect to their hosts. Since the luminosity of the host is roughly correlated with the mass of its central SMBH (e.g., Magorrian et al. 1998), this can probably be expressed as a bias towards AGN radiating at large fractions of their Eddington limits.

Finally, we have studied the distribution of AGN reddening in the WISE AGN candidates. We have shown that although WISE is more sensitive to unobscured objects, it still finds considerable numbers of highly obscured objects. Extending the sample to include all AGN found over the field with $\hat{a} > 0.5$, spectroscopic redshifts from the AGES survey, and high S/N WISE W2 fluxes, we have studied the distribution of objects as a function of AGN reddening. We present a formalism based on the step-wise maximum likelihood method of Efstathiou et al. (1988) designed to account for sample incompleteness as a function of obscuration. For a subsample of 362 objects with $I < 20$ and W2<15.73 for which the selection function is well understood, we find that the reddening distributions depend on AGN bolometric luminosity. The distribution is peaked for unobscured objects and then falls relatively monotonically towards $E(B-V) \sim 2$, raising towards higher values and then dropping again towards $E(B-V) \sim 10$. While it is possible that our small sample size could be driving some of the observed structure, we point out that this shape could be explained by continuous diffuse dust medium in which optically thick dust clouds are embedded. We find that when looking at the complete subsample, 47±8% of AGN are Type 1 ($E(B-V) < 0.15$; see §5.3). This fraction is a strong function of the AGN bolometric luminosity, consistent with the general scenario of a receding torus. At our lowest luminosity bin, centered at

$L_{\rm AGN} = 3 \times 10^{44}$ erg s^{-1}, we find a Type 1 fraction of 29±7%, which rises to 64±13% for the highest luminosity bin centered at $L_{\rm AGN} = 4 \times 10^{45}$ erg s^{-1}. Larger samples, such as that provided by the combination of SDSS and WISE, will provide greater constraints and insight into the dust distribution in AGN.

We would like to thank M. Dickinson, A.H. Gonzalez, J. Kartaltepe, B. Mobasher, H. Nayyeri, K. Penner and G. Zeimann for helping us obtain some of the Keck spectroscopic observations used in this work. We thank M. Elitzur for an insightful discussion about dust properties in AGN. We thank the NDWFS, NEWFIRM and MAGES survey teams for providing their respective data sets over the Boötes field. RJA and JW are supported by an appointment to the NASA Postdoctoral Program at the Jet Propulsion Laboratory, administered by Oak Ridge Associated Universities through a contract with NASA. This publication makes use of data products from the Wide-field Infrared Survey Explorer, which is a joint project of the University of California, Los Angeles, and the Jet Propulsion Laboratory/California Institute of Technology, funded by the National Aeronautics and Space Administration. Some of the data presented herein were obtained at the W.M. Keck Observatory, which is operated as a scientific partnership among the California Institute of Technology, the University of California and the National Aeronautics and Space Administration. The Observatory was made possible by the generous financial support of the W.M. Keck Foundation.

A. Additional Spectroscopic Redshifts in the NDWFS Boötes Field

The four slitmasks that we observed were designed to target WISE-selected AGN candidates in the Boötes field, though the low source density of such sources allowed for additional spectroscopic targets. We filled out the masks with: (1) IRAC-selected AGN candidates, using the two-color criteria of Stern et al. (2005) [Column 1 of table, *Target Type* = IRAC AGN]; (2) $z > 1$ galaxy cluster candidates from Eisenhardt et al. (2008) [*Target Type* = IRAC cluster]; (3) other 4.5 μm-selected sources from SDWFS, typically selected to have $[3.6]-[4.5] \geq -0.1$ (AB) which efficiently selects galaxies at $z > 1.2$ (e.g., Galametz et al. 2012) [*Target Type* = IRAC]; (4) X-ray sources from XBoötes (Murray et al. 2005; Kenter et al. 2005; Brand et al. 2006) [*Target Type* = XBoötes]; and (5) MIPS 24 μm sources in the field [*Target Type* = MIPS]. Given the interest and use of the Boötes field by a broad community, we include those additional sources here.

Table 6 presents the results for 129 Boötes sources for which we obtained redshifts, including the eleven targeted sources which are also listed in Table 5. The quality flags are

defined in §4.4. Of particular note is the LRIS mask which confirms cluster 10.220 from the catalog of Eisenhardt et al. (2008) to be at $z = 0.96$.

REFERENCES

Alonso-Herrero, A., et al. 2006, ApJ, 640, 167

Antonucci, R. 1993, ARA&A, 31, 473

Ashby, M. L. N., et al. 2009, ApJ, 701, 428

Assef, R. J., et al. 2010, ApJ, 713, 970

—. 2011, ApJ, 728, 56

Becker, R. H., White, R. L., & Helfand, D. J. 1995, ApJ, 450, 559

Bennert, V. N., Treu, T., Woo, J.-H., Malkan, M. A., Le Bris, A., Auger, M. W., Gallagher, S., & Blandford, R. D. 2010, ApJ, 708, 1507

Brand, K., et al. 2006, ApJ, 641, 140

Bridge, C. R., et al. 2012, ArXiv e-prints

Brodwin, M., et al. 2006, ApJ, 651, 791

Chung, S. M., et al. in prep.

Civano, F., et al. 2007, A&A, 476, 1223

Condon, J. J., Cotton, W. D., Greisen, E. W., Yin, Q. F., Perley, R. A., Taylor, G. B., & Broderick, J. J. 1998, AJ, 115, 1693

Cool, R. J. 2007, ApJS, 169, 21

Croton, D. J., et al. 2006, MNRAS, 365, 11

de Vries, W. H., Morganti, R., Röttgering, H. J. A., Vermeulen, R., van Breugel, W., Rengelink, R., & Jarvis, M. J. 2002, AJ, 123, 1784

Donley, J. L., et al. 2012, ApJ, 748, 142

Dullemond, C. P., & van Bemmel, I. M. 2005, A&A, 436, 47

Edelson, R., & Malkan, M. 2012, ApJ, 751, 52

Efstathiou, G., Ellis, R. S., & Peterson, B. A. 1988, MNRAS, 232, 431

Eisenhardt, P. R., et al. 2004, ApJS, 154, 48

Eisenhardt, P. R. M., et al. 2008, ApJ, 684, 905

—. 2012, ApJ, 755, 173

Elitzur, M., & Shlosman, I. 2006, ApJ, 648, L101

Elvis, M., et al. 2009, ApJS, 184, 158

Faber, S. M., et al. 2003, in Society of Photo-Optical Instrumentation Engineers (SPIE) Conference Series, Vol. 4841, Society of Photo-Optical Instrumentation Engineers (SPIE) Conference Series, ed. M. Iye & A. F. M. Moorwood, 1657–1669

Fabricant, D., et al. 2005, PASP, 117, 1411

Fan, X. 1999, AJ, 117, 2528

Fan, X., et al. 2006, AJ, 132, 117

Fazio, G. G., et al. 2004, ApJS, 154, 10

Feltre, A., Hatziminaoglou, E., Fritz, J., & Franceschini, A. 2012, ArXiv e-prints

Ferrarese, L., & Ford, H. 2005, Space Sci. Rev., 116, 523

Fritz, J., Franceschini, A., & Hatziminaoglou, E. 2006, MNRAS, 366, 767

Galametz, A., et al. 2012, ApJ, 749, 169

Glikman, E., Bogosavljević, M., Djorgovski, S. G., Stern, D., Dey, A., Jannuzi, B. T., & Mahabal, A. 2010, ApJ, 710, 1498

Glikman, E., Djorgovski, S. G., Stern, D., Dey, A., Jannuzi, B. T., & Lee, K.-S. 2011, ApJ, 728, L26

Gonzalez, A. H., et al. 2010, in American Astronomical Society Meeting Abstracts, Vol. 216, American Astronomical Society Meeting Abstracts #216, #415.13

Graham, A. W. 2007, MNRAS, 379, 711

—. 2012, ApJ, 746, 113

Grimes, J. A., Rawlings, S., & Willott, C. J. 2004, MNRAS, 349, 503

Hasinger, G. 2004, Nuclear Physics B Proceedings Supplements, 132, 86

Hopkins, P. F., Hernquist, L., Cox, T. J., Di Matteo, T., Martini, P., Robertson, B., & Springel, V. 2005, ApJ, 630, 705

Hopkins, P. F., Hernquist, L., Cox, T. J., & Kereš, D. 2008, ApJS, 175, 356

Jannuzi, B., et al. 2010, in Bulletin of the American Astronomical Society, Vol. 42, American Astronomical Society Meeting Abstracts #215, #470.01

Jannuzi, B. T., & Dey, A. 1999, in Astronomical Society of the Pacific Conference Series, Vol. 193, The Hy-Redshift Universe: Galaxy Formation and Evolution at High Redshift, ed. A. J. Bunker & W. J. M. van Breugel, 258

Jarrett, T. H., et al. 2011, ApJ, 735, 112

Kenter, A., et al. 2005, ApJS, 161, 9

Kochanek, C. S., et al. 2012, ApJS, 200, 8

Krolik, J. H., & Begelman, M. C. 1988, ApJ, 329, 702

Lacy, M., Petric, A. O., Sajina, A., Canalizo, G., Storrie-Lombardi, L. J., Armus, L., Fadda, D., & Marleau, F. R. 2007, AJ, 133, 186

Lacy, M., et al. 2004, ApJS, 154, 166

Lawrence, A. 1991, MNRAS, 252, 586

Lin, H., Kirshner, R. P., Shectman, S. A., Landy, S. D., Oemler, A., Tucker, D. L., & Schechter, P. L. 1996, ApJ, 464, 60

Magorrian, J., et al. 1998, AJ, 115, 2285

Maiolino, R., Marconi, A., Salvati, M., Risaliti, G., Severgnini, P., Oliva, E., La Franca, F., & Vanzi, L. 2001, A&A, 365, 28

Martin, D. C., et al. 2005, ApJ, 619, L1

Massey, P., & Gronwall, C. 1990, ApJ, 358, 344

Mateos, S., et al. 2012, MNRAS, in press.

Messias, H., Afonso, J., Salvato, M., Mobasher, B., & Hopkins, A. M. 2012, ApJ, 754, 120

Moran, E. C., Filippenko, A. V., & Chornock, R. 2002, ApJ, 579, L71

Murray, S. S., et al. 2005, ApJS, 161, 1

Nenkova, M., Ivezić, Ž., & Elitzur, M. 2002, ApJ, 570, L9

Nenkova, M., Sirocky, M. M., Ivezić, Ž., & Elitzur, M. 2008, ApJ, 685, 147

Oke, J. B., et al. 1995, PASP, 107, 375

Rengelink, R. B., Tang, Y., de Bruyn, A. G., Miley, G. K., Bremer, M. N., Roettgering, H. J. A., & Bremer, M. A. R. 1997, A&AS, 124, 259

Richards, G. T., et al. 2002, AJ, 123, 2945

—. 2006, ApJS, 166, 470

Rowan-Robinson, M., et al. 2008, MNRAS, 386, 697

Salvato, M., et al. 2009, ApJ, 690, 1250

Shakura, N. I., & Sunyaev, R. A. 1973, A&A, 24, 337

Simpson, C. 1998, MNRAS, 297, L39

—. 2005, MNRAS, 360, 565

Stengler-Larrea, E. A., et al. 1995, ApJ, 444, 64

Stern, D., Bunker, A., Spinrad, H., & Dey, A. 2000, ApJ, 537, 73

Stern, D., et al. 2005, ApJ, 631, 163

—. 2012, ApJ, 753, 30

Tristram, K. R. W., et al. 2007, A&A, 474, 837

Trump, J. R., et al. 2011, ApJ, 732, 23

Ueda, Y., Akiyama, M., Ohta, K., & Miyaji, T. 2003, ApJ, 598, 886

Urry, C. M., & Padovani, P. 1995, PASP, 107, 803

Wright, E. L., et al. 2010, AJ, 140, 1868

Wu, J., et al. 2012a, ApJ, 756, 96

Wu, X.-B., Hao, G., Jia, Z., Zhang, Y., & Peng, N. 2012b, AJ, 144, 49

This preprint was prepared with the AAS LaTeX macros v5.2.

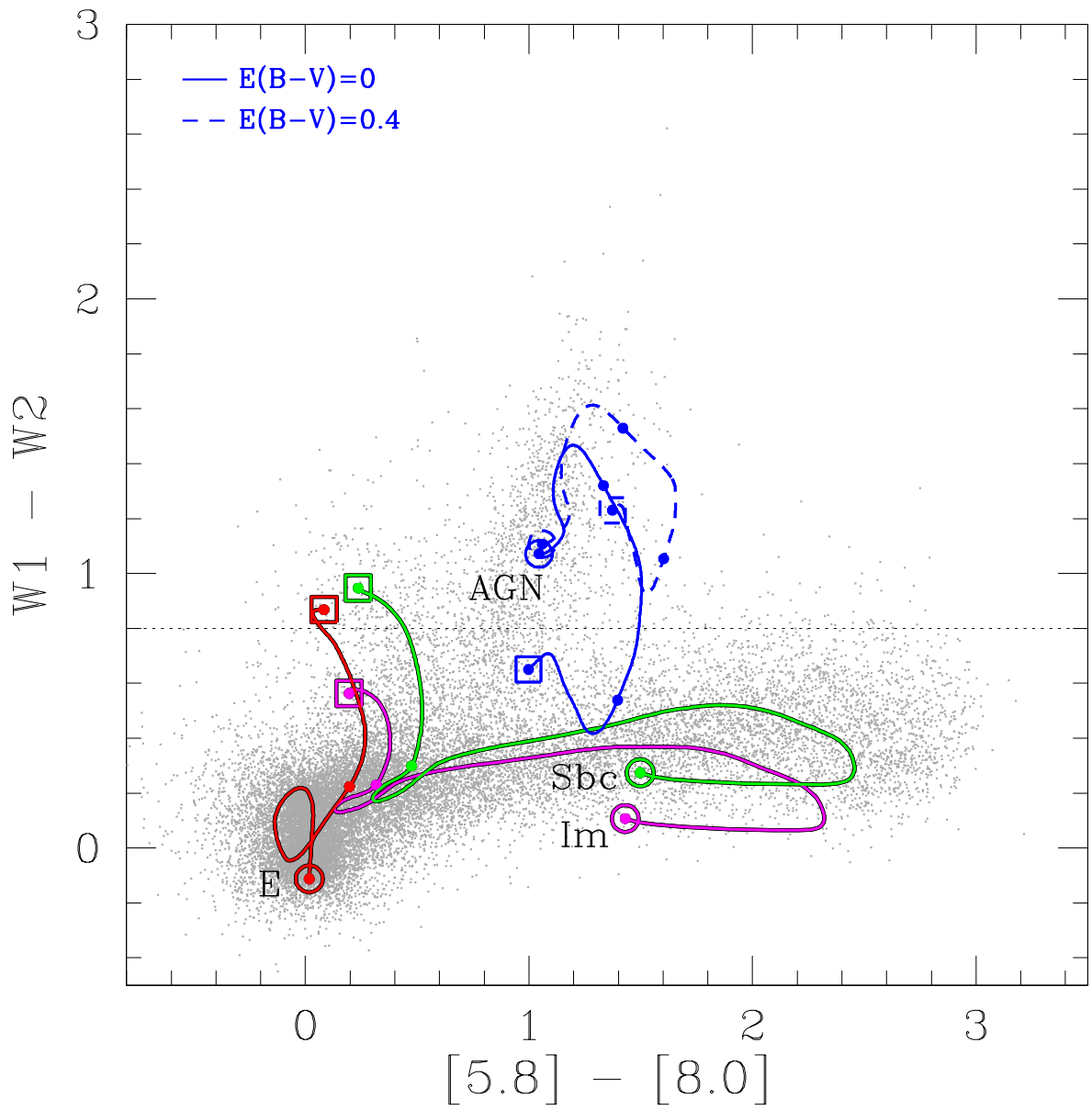

Fig. 1.— Distribution of [5.8]–[8.0] and W1–W2 colors in the Boötes field. The lines show the colors of the galaxy and AGN SED templates of Assef et al. (2010). The color of the galaxy templates E (*red line*), Sbc (*green line*) and Im (*magenta line*) are shown between redshifts 0 (*open circle*) and 2 (*open square*), with dots in the tracks in steps of $\Delta z = 1$. The AGN template is shown without reddening (*solid blue line*) and with $E(B-V) = 0.4$ (*dashed blue line*), in the redshift interval between $z = 0$ (*open circle*) and $z = 6$ (*open square*). Dots in the AGN color tracks are spaced by $\Delta z = 2$. The gray dots show all the WISE sources in the NDWFS field with $W2 < 15.73$.

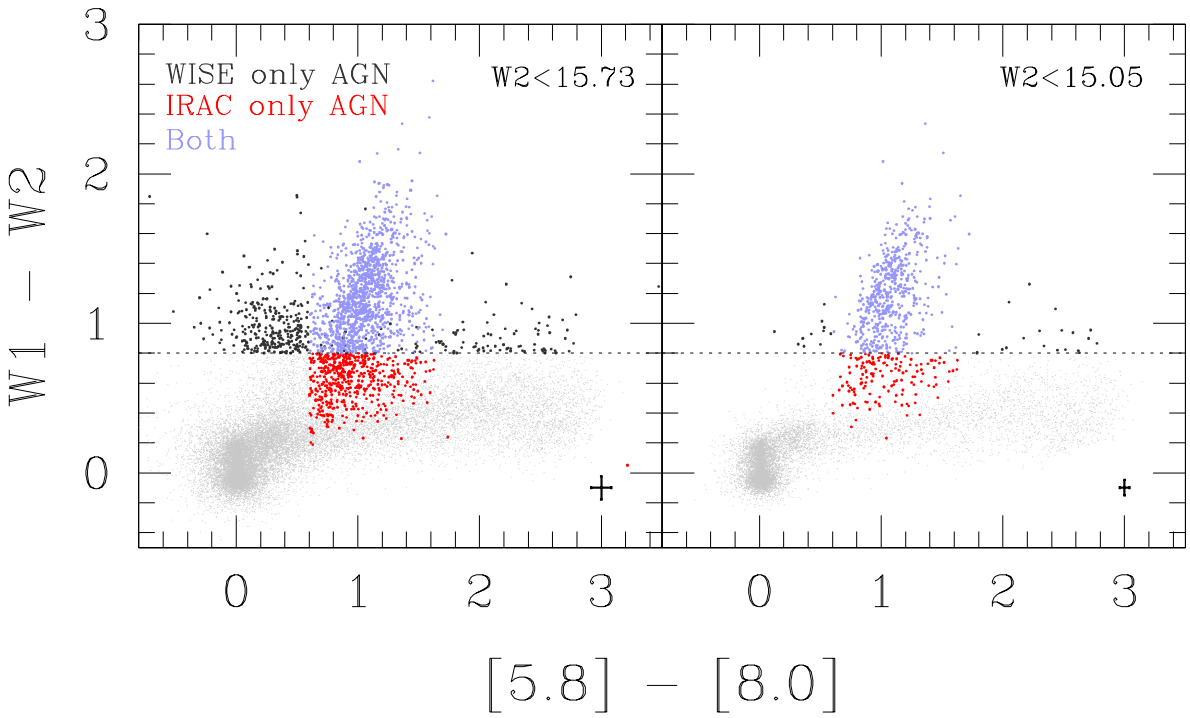

Fig. 2.— WISE W1–W2 versus SDWFS [5.8]–[8.0] colors for WISE sources in the NDWFS Boötes field. The left panel shows sources with W2 < 15.73, the 10σ WISE detection limit in the Boötes field, while the right panel shows sources limited to W2 < 15.05, corresponding to the W2 $S/N > 10$ limit in the COSMOS field. Objects are separated into non-AGN candidates (*light gray dots*), WISE and IRAC AGN candidates (*blue dots*), WISE-only candidates (*black dots*) and IRAC-only candidates (*red dots*). The median photometric uncertainty for each sample is shown in the lower right corner of each panel.

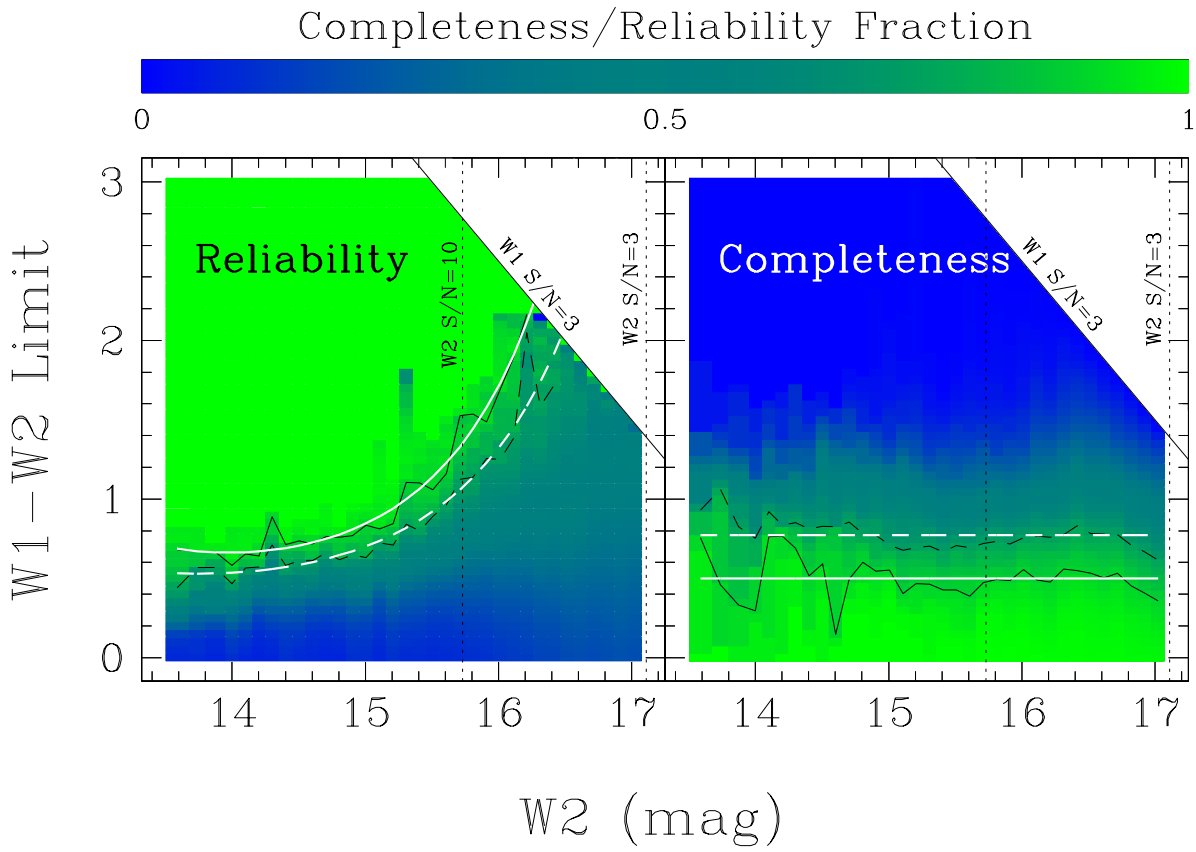

Fig. 3.— Reliability (*left panel*) and completeness (*right panel*) of AGN candidates defined by $\hat{a} > 0.5$ selected by a color cut on W1 − W2 as a function of W2 magnitude. Reliability and completeness of 90% (75%) are shown as a function of magnitude by the solid (dashed) black lines. Objects redder than the top right corner of the panels are missing due to the W1 $S/N > 3$ requirement. The proposed reliability-optimized criteria (eqn.[3]) for 90% (R_{90}) and 75% (R_{75}) reliability are shown in the left panel by the white solid and dashed lines, respectively. The completeness-optimized criteria (eqn.[4]) for 90% (C_{90}) and 75% (C_{75}) completeness are shown in the right panel with the same respective line styles.

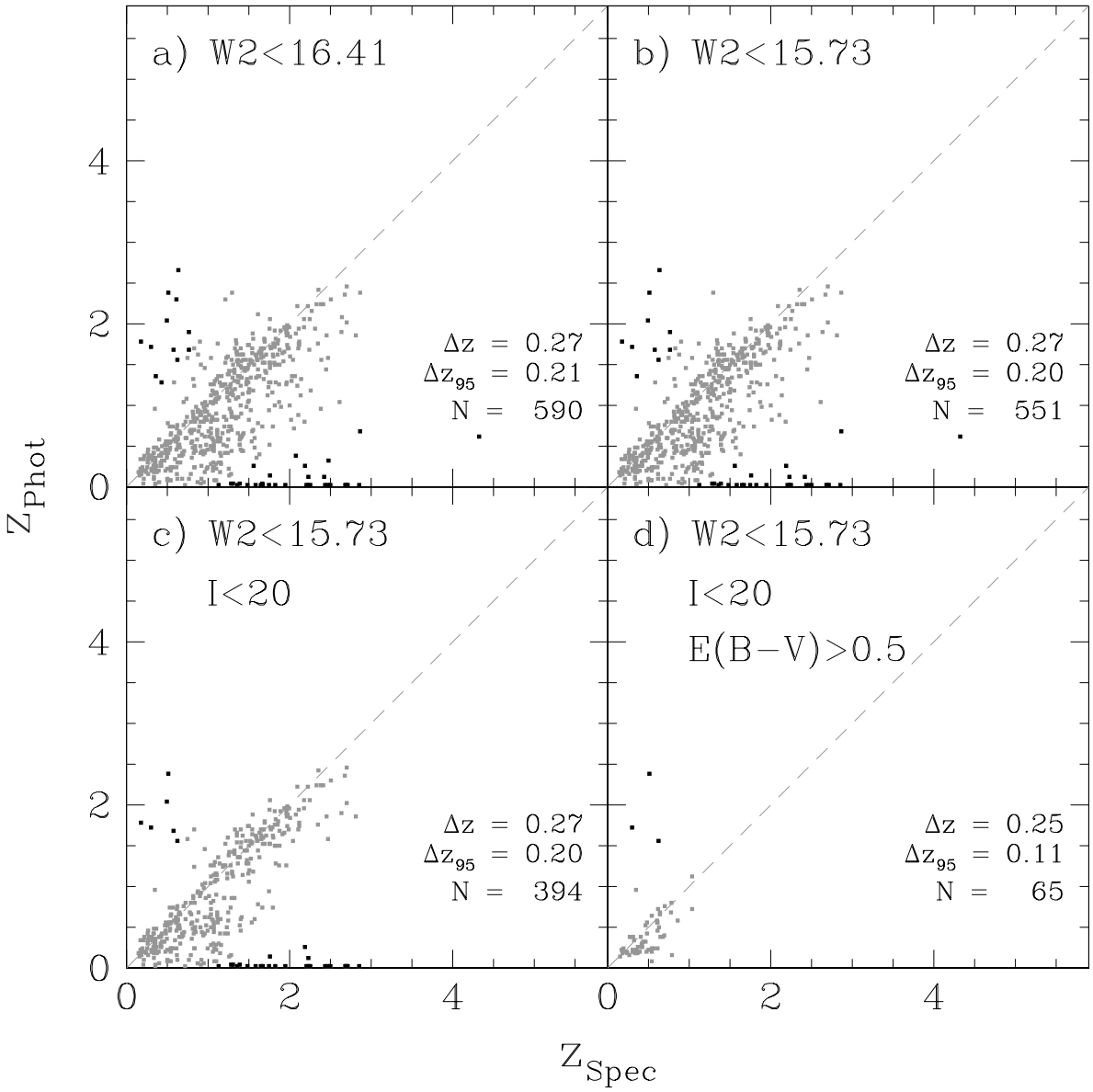

Fig. 4.— Comparison of photometric and spectroscopic redshifts for the R_{90} sample of AGN candidates for: *a)* the full W2 depth sample; *b)* limited to objects with W2 < 15.73; *c)* further limited to objects with $I < 20$; and *d)* even further limited to objects $E(B-V) > 0.5$. Each panel shows the dispersion between the photometric and spectroscopic redshifts for the full sample (Δz) and for the 95% objects with the best estimates to minimize the effect of outliers (Δz_{95}). Black points correspond to objects with $|(z_{\rm phot} - z_{\rm spec})/(1 + z_{\rm spec})| > 0.5$.

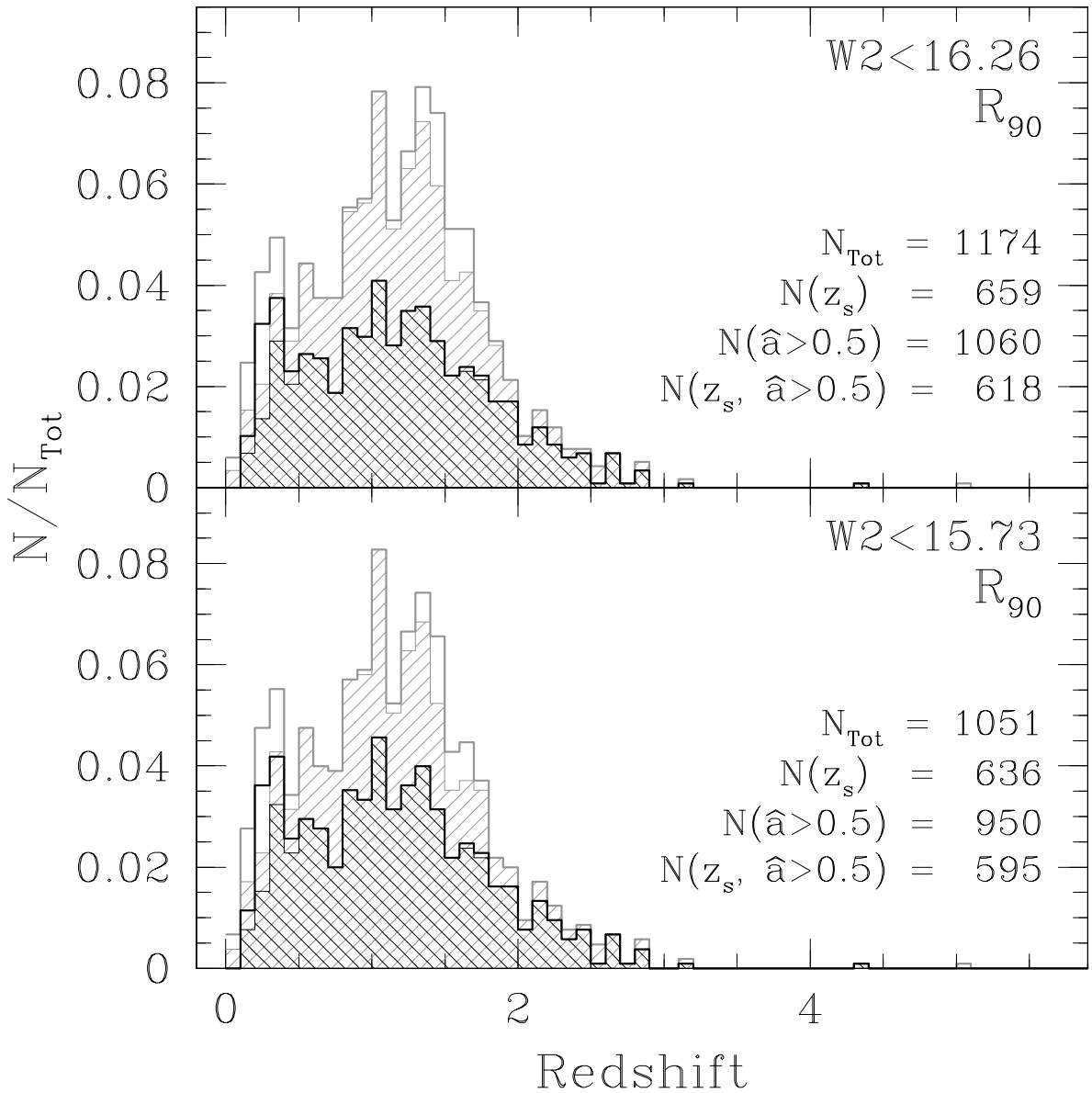

Fig. 5.— Redshift distribution of the R_{90} sample of AGN candidates for the full W2 depth of the field (*top panel*) and limited to objects with W2 $<$ 15.73 (*bottom panel*). Black histograms show objects with spectroscopic redshifts, while gray histograms add objects with photometric redshift estimates to the spectroscopic redshift histograms. Shaded histograms only include objects with $\hat{a} > 0.5$ while open histograms use objects with all $\hat{a}$ values, including the contaminants.

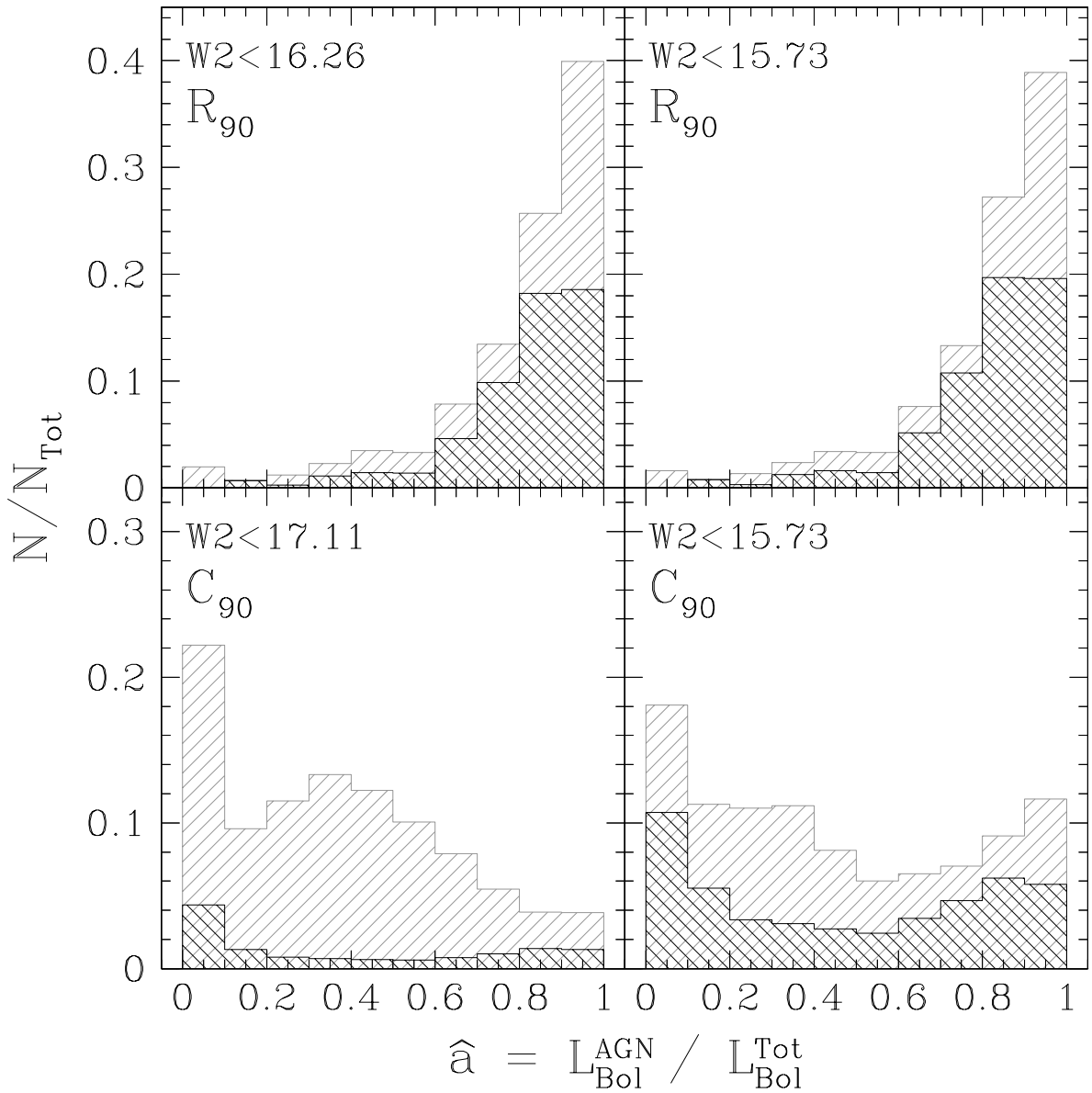

Fig. 6.— Distribution of $\hat{a}$ values for our R_{90} (*top*) and C_{90} (*bottom*) AGN candidate samples. Left panels show the full W2 depth samples, while the right panels are limited to objects with W2 < 15.73. Black histograms include only objects with spectroscopic redshifts, while gray histograms also include objects with photometric redshifts.

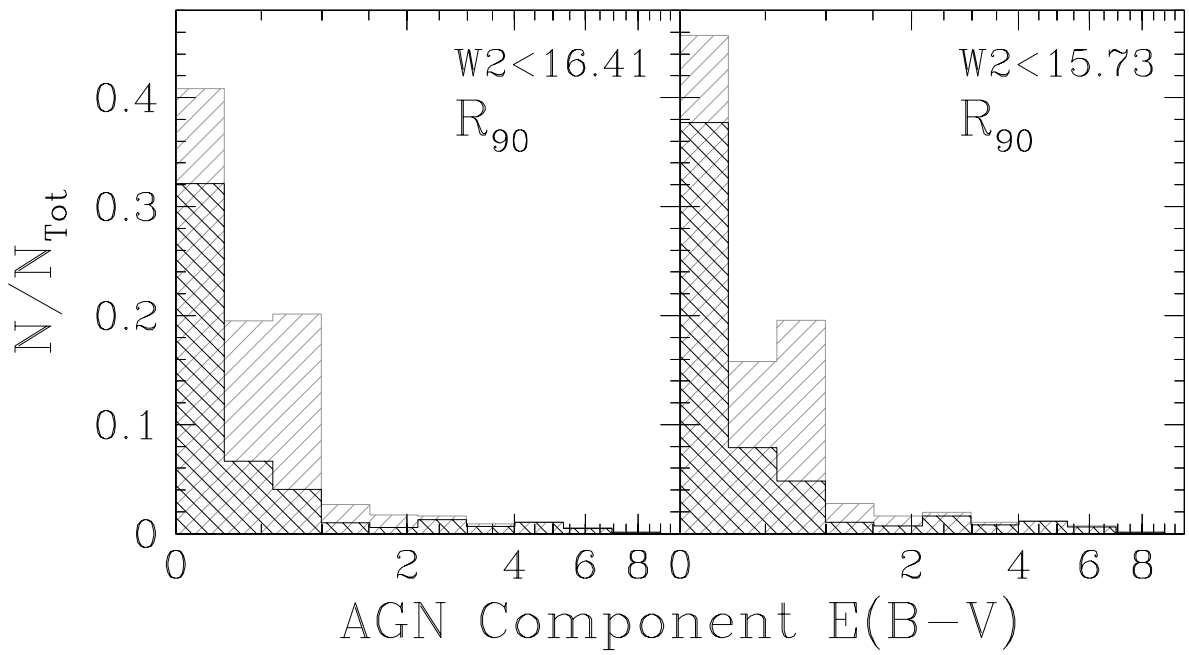

Fig. 7.— Distribution of best-fit AGN reddening $E(B-V)$ values for our R_{90} AGN candidate samples. Left panel shows the full W2 depth sample, while the right one is limited to objects with W2 < 15.73. Black histograms only include objects with spectroscopic redshifts, while gray histograms also include objects with photometric redshifts.

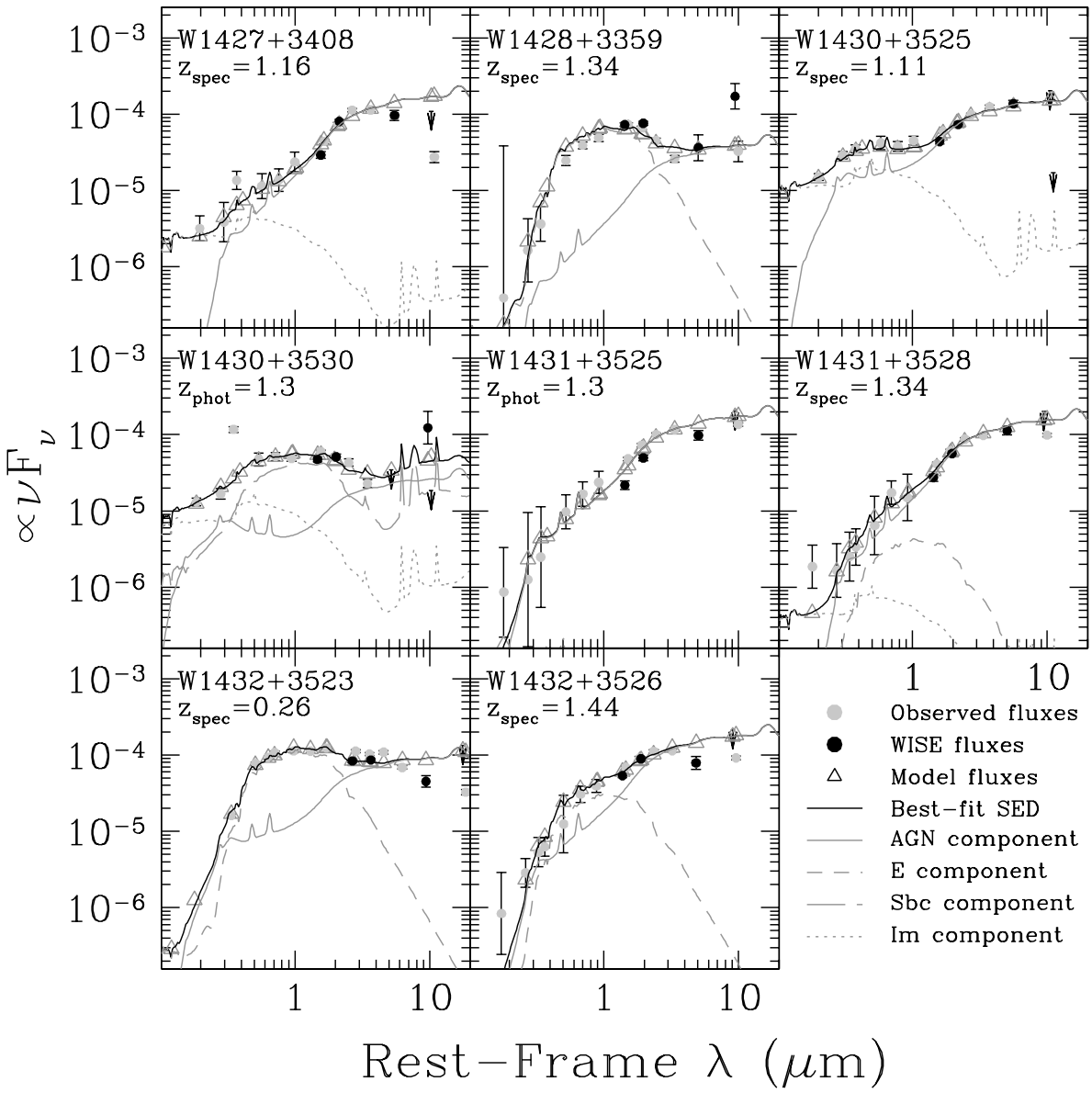

Fig. 8.— Best-fit SEDs for our sample of highly obscured, high-redshift AGN candidates observed with Keck. Only candidates that met one of the selection criteria beyond the very inclusive C_{90} when using the all-sky data release WISE photometry are shown.

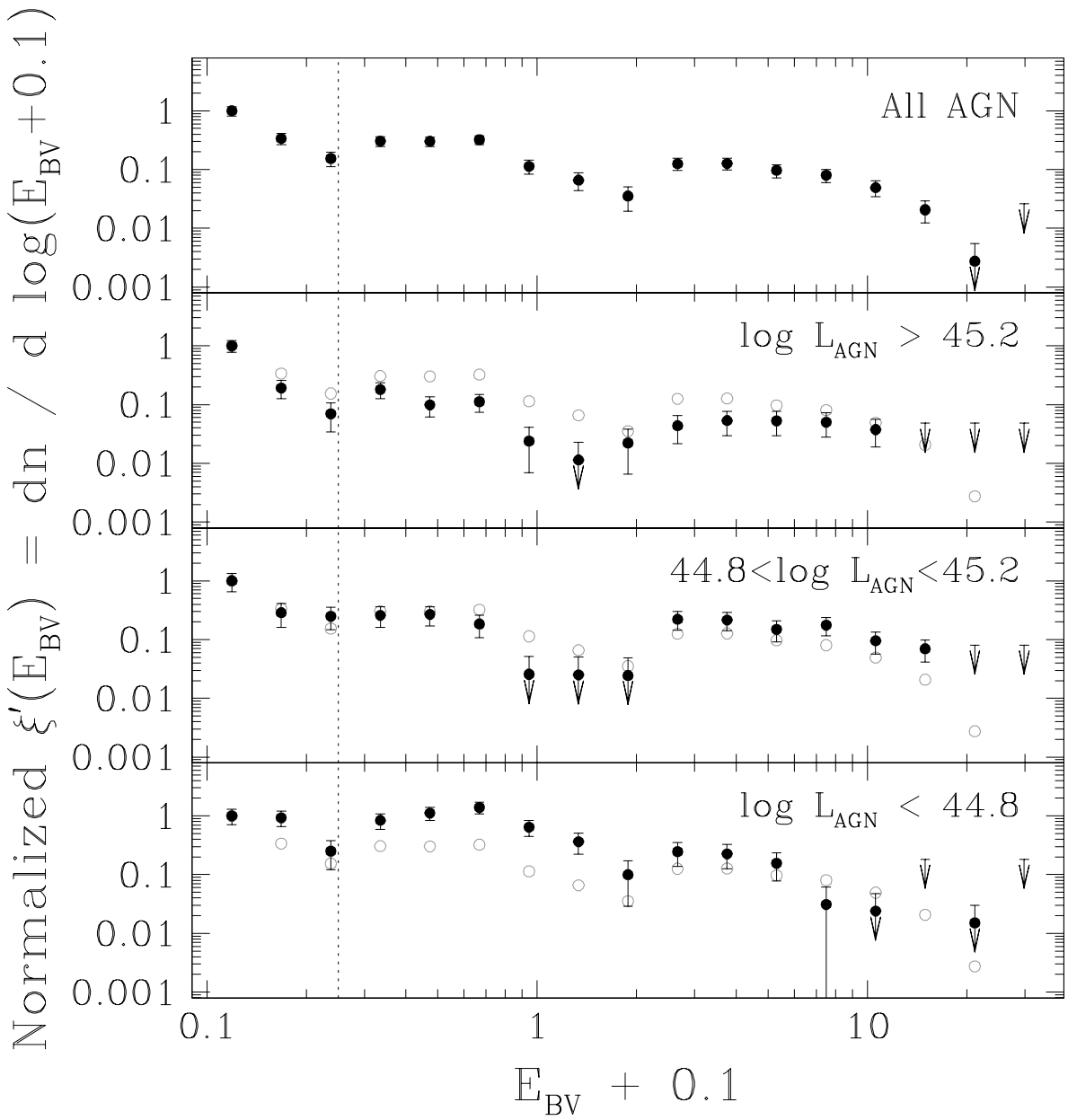

Fig. 9.— Distribution of reddening values (*solid black circles*) obtained after using the non-parametric formalism described in §5.2 to account for sample incompleteness. For simplicity, we adopt the notation $E_{BV} \equiv E(B-V)$. The top panel shows the distribution obtained when using the complete AGN sample, while the lower three panels show the distributions in three bins of AGN bolometric luminosity (erg s^{-1}) as defined in §2.3. The distribution obtained using all objects is repeated as open gray circles in each of the lower three panels for comparison. All the distributions are normalized to unity in the lowest E_{BV} bin. The vertical dotted line shows our adopted reddening boundary between Type 1 and Type 2 AGN.

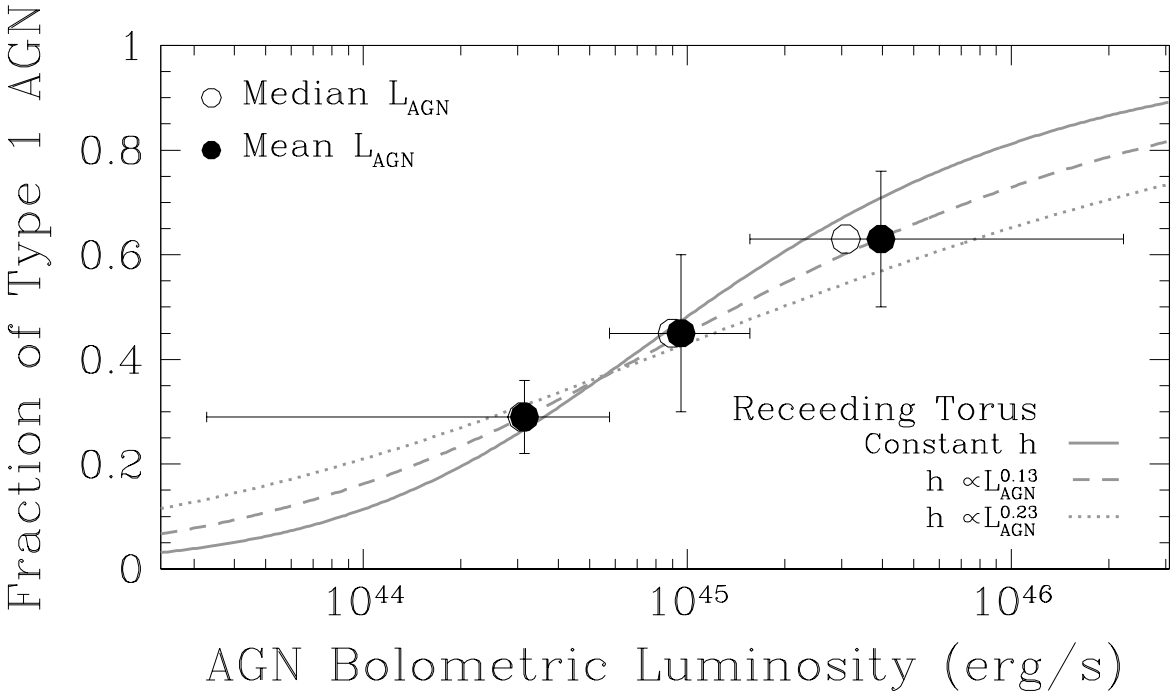

Fig. 10.— Type 1 AGN fraction as a function of AGN bolometric luminosity, as defined in §2.3. The solid points are centered at the mean AGN bolometric luminosity of the bin while the open ones are centered at the median value. The luminosity error-bars show the range of each luminosity bin. The gray lines shows the best-fit receding torus models described in the text.

Table 1. Surface Density of AGN Candidates at W2<17.11[†]

Selection Criterion	N (deg^{-2})	N ($\hat{a} > 0.5$) (deg^{-2})	Reliability Fraction	Completeness Fraction	Bands Used
WISE AGN Selection					
R_{90}	130	118	0.90	0.09	W1, W2
R_{75}	256	195	0.76	0.17	W1, W2
C_{90}	3702	1152	0.31	0.89	W1, W2
C_{75}	2117	929	0.44	0.72	W1, W2
W1–W2≥0.8*	2000	901	0.45	0.70	W1, W2
Jarrett et al. (2011)	469	268	0.57	0.21	W1, W2, W3[‡]
Mateos et al. (2012)	391	256	0.65	0.20	W1, W2, W3
—.	83	68	0.82	0.05	W1, W2, W3, W4
Assef et al. (2010)	1785	841	0.47	0.65	W1, W2
—.	44	43	0.97	0.03	W1, W2, W3, W4
Wu et al. (2012b)	3218	1109	0.34	0.86	W1, W2
Other Infrared AGN Selection					
Messias et al. (2012)	8206	1172	0.14	0.91	K_s, [4.5], [8.0]
—.	4227	783	0.19	0.60	K_s, [4.5], [8.0], MIPS 24μm
Stern et al. (2005)	986	659	0.67	0.51	[3.6], [4.5], [5.8], [8.0]
Lacy et al. (2004)	2888	1029	0.36	0.79	[3.6], [4.5], [5.8], [8.0]
Lacy et al. (2007)	1297	735	0.57	0.57	[3.6], [4.5], [5.8], [8.0]

[†]The effective W2 limits for the R_{90} and R_{75} criteria are 16.26 and 16.45 mag respectively due to the W1 $S/N > 3$ requirement of our sample.

[‡]W4 is also used if detected.

*This criterion corresponds to the color cut proposed by Paper I without the magnitude limit W2<15.05.

Note. — WISE AGN selection criteria R_{90}, R_{75}, C_{90} and C_{75} are described by eqns. (3) and (4). The remaining WISE AGN selection criteria are as follows: **Jarrett et al. (2011)**: W2–W3>2.2, W2–W3>4.2, W1–W2>0.1(W2–W3)+0.38, W1–W2<1.7 and object is not a star; **Mateos et al. (2012) 3-band**: W2–W3>2.157, W1–W2>0.315(W2–W3)–0.222, W1–W2<0.315(W2–W3)+0.796; **Mateos et al. (2012) 4-band**: W3–W4≥1.76, W1–W2>0.50(W3–W4)–0.405, W1–W2<0.50(W3–W4)+0.979; **Assef et al. (2010) 2-band**: W1–W2>0.85; **Assef et al. (2010) 4-band**: W3–W4>2.1, W1–W2>0.85, W1–W2>1.67(W3–W4)–3.41; **Wu et al. (2012b)**: W1–W2>0.57. For the other infrared AGN selection criteria we refer the reader to the original studies.

Table 2. Surface Density of AGN Candidates at W2<15.73

Selection Criterion	N (deg^{-2})	N ($\hat{a} > 0.5$) (deg^{-2})	Reliability Fraction	Completeness Fraction	Bands Used
WISE AGN Selection					
R_{90}	117	106	0.90	0.53	W1, W2
R_{75}	176	133	0.76	0.67	W1, W2
C_{90}	439	177	0.40	0.88	W1, W2
C_{75}	194	144	0.74	0.72	W1, W2
W1–W2≥0.8*	182	139	0.77	0.69	W1, W2
Jarrett et al. (2011)	166	128	0.77	0.64	W1, W2, W3‡
Mateos et al. (2012)	161	129	0.80	0.64	W1, W2, W3
—.	69	56	0.80	0.28	W1, W2, W3, W4
Assef et al. (2010)	161	130	0.81	0.65	W1, W2
—.	39	38	0.98	0.19	W1, W2, W3, W4
Wu et al. (2012b)	347	170	0.49	0.85	W1, W2
Other Infrared AGN Selection					
Messias et al. (2012)	2116	184	0.09	0.92	K_s, [4.5], [8.0]
—.	955	163	0.17	0.81	K_s, [4.5], [8.0], MIPS 24μm
Stern et al. (2005)	194	157	0.81	0.79	[3.6], [4.5], [5.8], [8.0]
Lacy et al. (2004)	484	183	0.38	0.92	[3.6], [4.5], [5.8], [8.0]
Lacy et al. (2007)	262	172	0.66	0.86	[3.6], [4.5], [5.8], [8.0]

‡W4 is also used if detected.

*This criterion corresponds to the color cut proposed by Paper I without the magnitude limit W2<15.05.

Table 3. Surface Density of AGN Candidates at W2<15.05

Selection Criterion	N (deg^{-2})	N ($\hat{a} > 0.5$) (deg^{-2})	Reliability Fraction	Completeness Fraction	Bands Used
WISE AGN Selection					
R_{90}	66	59	0.90	0.77	W1, W2
R_{75}	87	65	0.75	0.84	W1, W2
C_{90}	120	69	0.57	0.89	W1, W2
C_{75}	64	59	0.93	0.77	W1, W2
Paper I	62	58	0.94	0.75	W1, W2
Jarrett et al. (2011)	66	59	0.90	0.77	W1, W2, W3[‡]
Mateos et al. (2012)	65	60	0.92	0.78	W1, W2, W3
—.	48	39	0.82	0.51	W1, W2, W3, W4
Assef et al. (2010)	57	55	0.96	0.71	W1, W2
—.	29	29	1.00	0.37	W1, W2, W3, W4
Wu et al. (2012b)	99	67	0.68	0.87	W1, W2
Other Infrared AGN Selection					
Messias et al. (2012)	952	70	0.07	0.91	K_s, [4.5], [8.0]
—.	323	65	0.20	0.84	K_s, [4.5], [8.0], MIPS 24μm
Stern et al. (2005)	74	66	0.89	0.85	[3.6], [4.5], [5.8], [8.0]
Lacy et al. (2004)	123	70	0.56	0.90	[3.6], [4.5], [5.8], [8.0]
Lacy et al. (2007)	91	68	0.75	0.89	[3.6], [4.5], [5.8], [8.0]

[‡]W4 is also used if detected.

Table 4. Photometric Redshifts

Sample	Δz	Δz_{95}	bias/$(1+z)$	bias$^{95\%}/(1+z)$	N_{AGN}	z_s Fraction
Full W2 Depth						
R_{90}	0.27	0.20	0.15	0.14	618	0.56
R_{75}	0.29	0.21	0.14	0.13	839	0.44
C_{90}	0.31	0.23	0.13	0.12	1668	0.13
C_{75}	0.29	0.23	0.17	0.16	1360	0.10
W2<15.73						
R_{90}	0.27	0.20	0.14	0.13	595	0.61
R_{75}	0.29	0.20	0.13	0.12	731	0.57
C_{90}	0.29	0.19	0.09	0.09	890	0.48
C_{75}	0.26	0.20	0.13	0.12	740	0.48
W2<15.73 and I<20						
R_{90}	0.27	0.20	0.13	0.12	420	0.85
R_{75}	0.30	0.20	0.12	0.11	507	0.84
C_{90}	0.30	0.19	0.09	0.09	597	0.75
C_{75}	0.27	0.20	0.13	0.12	477	0.82
W2<15.73 and I<20 and $E(B-V)$>0.5						
R_{90}	0.25	0.11	0.10	0.11	68	0.77
R_{75}	0.42	0.12	0.09	0.10	90	0.84
C_{90}	0.42	0.11	0.04	0.05	134	0.76
C_{75}	0.24	0.12	0.11	0.12	78	0.78

Table 5. Summary of Obscured AGN Candidates Observed with Keck/DEIMOS

Name	R.A.	Dec.	I (mag)	W2 (mag)	W1–W2	$\hat{a}$	$E(B-V)$	z	Q	Selection	Notes
W1427+3400	14:27:54.57	34:00:43.31	21.90	15.81	0.82	0.386 ± 0.091	0.41± 0.11	1.29	A	C_{75}	[O II]
W1427+3403	14:27:47.16	34:03:41.84	21.24	15.76	0.50	0.209 ± 0.117	0.33± 0.12	1.14	A	*None*	CaHK
W1427+3408	14:27:17.93	34:08:28.60	21.71	14.99	2.08	0.989 ± 0.009	0.88± 0.04	1.16	A	R_{90}	[O II]
W1428+3359	14:28:12.31	33:59:25.13	23.22	15.15	1.02	0.685 ± 0.027	0.87± 0.05	1.34	B	R_{90}	[O II]
W1429+3529	14:29:54.83	35:29:04.08	21.97	15.77	0.71	0.455 ± 0.082	0.20± 0.08	(1.3)	F	C_{90}	
W1430+3525	14:30:31.69	35:25:17.78	20.64	15.07	1.54	0.944 ± 0.012	0.45± 0.06	1.11	A	R_{90}	[O II],CaHK
W1430+3530	14:30:00.50	35:30:55.01	19.42	15.55	1.06	0.497 ± 0.044	0.25± 0.07	(1.3)	F	R_{75}	
W1431+3525	14:31:06.26	35:25:46.24	23.63	15.60	1.88	1.000 ± 0.004	0.78± 0.05	(1.3)	C	R_{90}	[O II]
W1431+3528	14:31:31.38	35:28:38.21	23.62	15.47	1.77	0.990 ± 0.004	0.89± 0.04	1.34	A	R_{90}	[O II]
W1432+3523	14:32:23.02	35:23:21.41	19.03	14.33	1.01	0.742 ± 0.006	0.50± 0.03	0.26	A	R_{90}	CaHK,Hα,[N II]
W1432+3525	14:32:37.30	35:25:12.56	21.94	15.54	0.72	0.583 ± 0.036	0.75± 0.05	1.12	A	C_{90}	Mg II absn,[O II],D4000
W1432+3526	14:32:22.61	35:26:46.88	22.85	15.01	1.53	0.954 ± 0.006	0.79± 0.05	1.44	B	R_{90}	[O II]

Note. — The AGN selection criteria listed in the last column is the least inclusive one met. For sources that failed to yield spectroscopic redshifts in these observations, we list the photometric redshift in parenthesis. Coordinates are J2000.

Table 6. Additional Results from Keck Observations.

Target Type	R.A.	Dec.	z	Q	Slitmask(s)	Notes
IRAC	14:27:13.39	+34:09:04.5	1.343	A	C[36]	Mg II absorption,[O II]
IRAC AGN	14:27:14.32	+34:09:01.3	1.692	B	C[14]	QSO: Mg II (w/ Mg II absorption system at z=1.342)
MIPS	14:27:14.63	+34:08:46.6	1.343	B	C[33]	QSO: Mg II
MIPS	14:27:14.77	+34:06:09.0	1.151	A	C[28]	Mg II absorption,[O II],D4000
MIPS	14:27:17.40	+34:07:26.9	1.082	A	C[31]	[O II],[Ne III]
WISE AGN	14:27:17.92	+34:08:28.6	1.158	A	C[03]	[O II]
MIPS	14:27:18.37	+34:09:01.3	0.130	A	C[34]	[O III],Hα
IRAC	14:27:19.18	+34:06:47.0	1.213	B	C[37]	[O II],D4000
IRAC	14:27:20.76	+34:06:42.8	0.305	A	C[38]	Hβ,[O III],Hα
MIPS	14:27:23.95	+34:06:15.5	0.190	A	C[29]	Hβ,[O III],Hα
XBoötes	14:27:24.80	+34:05:12.7	1.753	A	C[15]	QSO: C III],Mg II
IRAC	14:27:27.55	+34:05:38.1	1.483	A	C[40]	B2900,[O II]
MIPS	14:27:27.56	+34:04:13.7	0.126	A	C[23]	Hβ,[O III],Hα
IRAC	14:27:27.90	+34:06:25.5	1.690	B	C[41]	Mg II absorption,[O II] (do not see past 1μm in Allslits, to confirm [O II])
MIPS	14:27:29.76	+34:04:34.8	1.065	A	C[25]	[O II],D4000
MIPS	14:27:30.15	+34:06:05.0	0.191	A	C[27]	Hβ,[O III],Hα
IRAC AGN	14:27:31.50	+34:03:28.6	2.192	A	C[13]	QSO2: C IV,He II,C III]
IRAC	14:27:32.07	+34:03:19.4	1.413	A	C[42]	[O II]
MIPS	14:27:32.42	+34:08:08.0	0.872	A	C[32]	[O II],D4000
IRAC	14:27:41.87	+34:04:55.0	1.524	A	C[43]	Mg II absorption,[O II]
IRAC AGN	14:27:43.36	+34:03:06.1	3.134	A	C[12]	QSO: Lyα,C IV,C III] (self-absorbed)
WISE AGN	14:27:47.17	+34:03:41.2	1.137	A	C[02]	CaHK
serendip	14:27:47.26	+34:03:40.8	1.623	B	C[02]	[O II] - v. ft. serendipitous
IRAC AGN	14:27:47.98	+34:02:44.1	3.276	A	C[11]	QSO: Lyα,C IV,C III]
IRAC	14:27:48.28	+34:03:11.7	1.427	A	C[45]	[O II]

Table 6—Continued

Target Type	R.A.	Dec.	z	Q	Slitmask(s)	Notes
WISE AGN	14:27:54.60	+34:00:43.0	1.293	A	C[01]	[O II]
MIPS	14:27:55.18	+34:02:41.9	0.643	A	C[22]	[O II],Hβ,[O III]
IRAC	14:27:57.49	+34:03:50.8	0.494	A	C[35]	[O II],CaHK,Hβ,Hα
IRAC	14:27:59.64	+34:03:07.3	1.621	A	C[49]	[O II]
MIPS	14:28:03.55	+33:59:23.4	0.756	A	C[18]	[O II],CaHK,Hβ
MIPS	14:28:03.65	+34:02:25.3	0.679	A	C[20]	[O II],Hβ,[O III]
MIPS	14:28:04.84	+34:02:27.8	0.458	A	C[21]	[O II],Hβ,[O III],Hα
MIPS	14:28:07.73	+33:58:28.9	1.262	A	C[17]	QSO: Mg II,[O II],[Ne III]
MIPS	14:28:09.59	+34:01:31.6	0.627	A	C[19]	[O II],Hβ,[O III]
MIPS	14:28:09.71	+33:58:06.6	1.246	A	C[16]	[O II]
XBoötes	14:28:10.07	+34:28:19.4	1.234	A	F	AGN: C III],[O II]
IRAC	14:28:11.28	+34:00:54.6	1.484	A	C[53]	[O II]
WISE AGN	14:28:12.30	+33:59:25.6	1.343	B	C[00]	[O II]
IRAC	14:28:14.26	+34:29:22.5	0.607	A	F	AGN
IRAC cluster	14:28:14.91	+34:28:28.2	1.08	B	F	D4000
IRAC cluster	14:28:15.24	+34:27:35.1	1.023	B	F	[O II]
IRAC	14:28:19.56	+34:23:10.0	0.363	A	F	[O II],Hα
IRAC cluster	14:28:21.26	+34:28:52.3	0.962	A	F	Mg II absorption,[O II],D4000,Hδ
IRAC cluster	14:28:22.15	+34:27:36.4	1.140	A	F	[O II],CaHK
IRAC cluster	14:28:22.34	+34:27:21.6	0.963	A	F	CaHK
IRAC cluster	14:28:23.63	+34:27:17.5	0.96	B	F	D4000
WISE AGN	14:28:25.03	+34:22:37.2	1.518	B	F	[O II]
IRAC cluster	14:28:25.06	+34:26:59.5	0.963	B	F	CaK,D4000
IRAC cluster	14:28:25.86	+34:25:33.4	0.95	B	F	D4000
XBoötes	14:28:29.06	+34:25:45.6	1.036	A	F	AGN: broad Mg II,[Ne V],[O II],[O III]

Table 6—Continued

Target Type	R.A.	Dec.	z	Q	Slitmask(s)	Notes
IRAC	14:28:30.21	+34:27:33.8	0.424	A	F	Mg II absorption,Hα
IRAC	14:28:31.10	+34:24:28.7	3.333	B	F	asymmetric Lyα, Lyα break
IRAC	14:28:37.32	+34:24:50.5	1.049	A	F	[O II],D4000
IRAC	14:28:40.39	+34:24:21.0	0.694	A	F	AGN: broad Mg II,narrow Hβ,[O III]
MIPS	14:29:55.16	+35:30:26.2	0.632	A	A[45]	[O II],Hβ,[O III] (Hβ w/ 2nd component)
XBoötes	14:29:57.10	+35:30:54.5	0.264	A	A[15]	QSO: Hβ,[O III],Hα
serendip	14:29:57.69	+35:27:42.4	0.492	A	A[39]	[O II],[O III]
MIPS	14:29:57.94	+35:27:42.1	0.547	A	A[39]	[O II],Hβ,[O III]
IRAC	14:29:58.94	+35:29:27.9	1.576	B	A[51]	[O II]
IRAC	14:30:06.07	+35:31:10.6	1.275	B	A[52]	CaHK
MIPS	14:30:07.83	+35:29:28.0	1.004	A	A[43]	[O II],D4000
IRAC	14:30:08.78	+35:30:51.3	1.092	A	A[53]	[O II],D4000
MIPS	14:30:09.20	+35:28:54.3	0.059	A	A[41]	Hβ,[O III],Hα,[S III]
IRAC AGN	14:30:09.55	+35:28:22.3	0.978	A	A[14]	QSO-2: lots of lines, including [Ne V]3426
IRAC	14:30:11.03	+35:27:08.1	3.156	B	A[54]	Lyα (serendipitous?)
MIPS	14:30:12.50	+35:27:14.6	0.177	A	A[36]	Hβ,[O III],Hα
MIPS	14:30:13.14	+35:26:53.7	0.362	A	A[33]	CaHK
MIPS	14:30:14.33	+35:26:49.4	1.481	A	A[32]	AGN: [Ne V],[O II],[Ne III]
MIPS	14:30:16.54	+35:30:41.9	0.792	A	A[47]	[O II],Hβ,[O III]
IRAC AGN	14:30:19.78	+35:27:04.7	1.268	A	A[13]	AGN: [Ne V]3426,[O II]
MIPS	14:30:20.75	+35:26:50.3	0.681	A	A[31]	CaHK
MIPS	14:30:21.18	+35:29:12.7	0.0	A	A[42]	M-star
IRAC	14:30:25.05	+35:27:28.8	0.351	A	A[49]	CaHK,Hα,[N II] (AGN based on [N II]/Hα ratio?)
serendip	14:30:25.56	+35:26:28.4	0.664	A	A[29]	[O II],Hβ,[O III]
MIPS	14:30:26.03	+35:28:42.4	0.264	A	A[40]	Hβ,[O III],Hα ([O II] in 2nd order?)

Table 6—Continued

Target Type	R.A.	Dec.	z	Q	Slitmask(s)	Notes
MIPS	14:30:26.34	+35:26:22.2	0.940	A	A[29]	[O II],CaHK
MIPS	14:30:26.96	+35:26:05.8	0.349	A	A[27]	[O II],CaHK,Hβ,[O III],Hα
MIPS	14:30:30.74	+35:25:42.8	1.024	A	A[24]	[O II]
WISE AGN	14:30:31.71	+35:25:17.8	1.106	A	A[00]	[O II],CaHK
serendip	14:30:31.92	+35:25:17.4	0.153	A	A[00]	[O III],Hα,[S II]
MIPS	14:30:32.32	+35:27:06.2	1.025	A	A[35]	[O II],D4000
MIPS	14:30:37.25	+35:26:37.1	1.012	A	A[30]	QSO: broad Mg II,[O II],Hβ,[O III]
serendip	14:30:37.26	+35:27:38.2	0.524	A	A[38]	[O II],Hβ,[O III] (or target?)
IRAC	14:30:38.10	+35:24:47.1	1.305	A	A[56]	[O II]
WISE AGN	14:30:42.92	+35:28:14.7	1.395	B	A[02]	[O II]
MIPS	14:30:46.02	+35:24:50.4	0.308	A	A[20]	[O II],Hβ,[O III],Hα
MIPS	14:30:48.46	+35:27:02.4	0.375	A	A[34]	CaHK,Hα
IRAC AGN	14:30:51.09	+35:24:08.0	2.043	A	A[11]	QSO: C IV,C III],Mg II
serendip	14:30:51.34	+35:24:07.2	0.0	A	A[11]	star: Hα,CaT absorption
IRAC AGN	14:30:51.46	+35:25:49.4	0.321	A	A[12]	CaHK
MIPS	14:30:56.51	+35:25:40.8	0.720	A	A[23]	[O II],Balmer absorption,Hβ,[O III]
MIPS	14:31:00.30	+35:25:46.0	0.084	A	A[25]	Hβ,[O III],Hα
MIPS	14:31:01.91	+35:24:48.6	0.650	A	A[19]	AGN: [Ne V]3426,[O II],Hβ,[O III]
MIPS	14:31:02.47	+35:24:34.5	0.651	A	A[18]	[O II],Hβ,[O III]
serendip	14:31:05.86	+35:24:00.6	0.414	A	A[48]	Hβ,[O III],Hα
IRAC	14:31:06.00	+35:23:59.4	0.429	A	A[48]	Hβ,[O III]
WISE AGN	14:31:31.39	+35:28:38.3	1.343	A	B[03]	[O II]
IRAC AGN	14:31:34.52	+35:29:23.3	1.210	A	B[15]	QSO-2: lots of lines
MIPS	14:31:34.83	+35:27:46.6	0.485	A	B[33]	[O II],Hβ
serendip	14:31:36.26	+35:29:18.9	0.163	A	B[40]	Hβ,[O III],Hα

Table 6—Continued

Target Type	R.A.	Dec.	z	Q	Slitmask(s)	Notes
IRAC	14:31:39.75	+35:28:01.4	1.028	A	B[42]	[O II]
MIPS	14:31:41.00	+35:28:11.9	0.958	A	B[35]	[O II]
MIPS	14:31:41.18	+35:29:44.8	0.163	A	B[41]	[O III],[N II],[S II]
serendip	14:31:41.32	+35:28:09.6	1.101	A	B[35]	[O II]
MIPS	14:31:41.87	+35:27:49.5	0.820	A	B[34]	[O II],Hβ,[O III]
MIPS	14:31:44.23	+35:27:43.3	0.0	A	B[32]	star: CaT
MIPS	14:31:47.43	+35:28:51.2	0.243	A	B[39]	[O II],Hα
MIPS	14:31:48.57	+35:28:15.5	1.215	A	B[36]	[O II]
IRAC	14:31:52.06	+35:28:21.2	0.765	A	B[43]	[O II],CaHK,[O III]
serendip	14:31:53.61	+35:26:26.5	0.0	A	B[49]	M-star
IRAC AGN	14:31:55.50	+35:26:40.3	0.911	A	B[14]	QSO: [O II],CaHK,[O III],broad Hα
serendip	14:31:58.55	+35:25:51.6	1.136	A	B[51]	[O II]
IRAC	14:31:58.85	+35:25:49.0	2.957	A	B[51]	ft. QSO: Lyα,C IV,He II,C III]
MIPS	14:31:59.27	+35:26:46.2	0.369	A	B[26]	[O II],Hα
IRAC	14:31:59.54	+35:28:21.9	0.557	A	B[44]	CaHK
MIPS	14:32:01.73	+35:28:46.0	0.392	A	B[38]	Hβ,[O III],Hα
MIPS	14:32:03.08	+35:26:46.7	0.336	A	B[27]	Hβ,[O III],Hα
serendip	14:32:04.97	+35:26:42.4	0.438	A	B[27]	[O II],CaHK,Hα
MIPS	14:32:06.77	+35:25:08.0	0.732	A	B[24]	[O II],Hβ,[O III]
IRAC AGN	14:32:11.50	+35:25:34.6	0.307	A	B[12]	CaHK,Hβ,[O III],Hα
IRAC	14:32:13.37	+35:27:10.5	0.0	A	B[45]	star: CaT
IRAC	14:32:17.71	+35:25:21.7	0.368	A	B[46]	[O II],CaHK,Hβ,Hα
serendip	14:32:18.14	+35:25:19.3	1.136	A	B[46]	[O II]
MIPS	14:32:19.72	+35:24:26.5	0.666	A	B[23]	[O II],Hβ,[O III]
WISE AGN	14:32:22.64	+35:26:46.7	1.436	B	B[02]	[O II] (bad slitlet)

Table 6—Continued

Target Type	R.A.	Dec.	z	Q	Slitmask(s)	Notes
WISE AGN	14:32:23.06	+35:23:21.4	0.258	A	B[00]	CaHK,Hα,[N II] (likely AGN from Hα/[N II] ratio)
MIPS	14:32:26.08	+35:27:14.7	0.662	A	B[28]	[O II],Hβ
MIPS	14:32:27.84	+35:22:42.0	0.469	A	B[20]	[O II],Hβ,[O III],Hα
MIPS	14:32:28.30	+35:27:35.1	0.380	A	B[30]	CaHK,Hβ,[O III],Hα
MIPS	14:32:29.30	+35:22:36.0	1.011	A	B[18]	[O II],D4000
IRAC	14:32:29.80	+35:26:29.5	1.136	A	B[48]	Mg II absorption,[O II]
XBoötes	14:32:32.03	+35:26:26.6	1.077	A	B[16]	[O II],CaHK
IRAC AGN	14:32:36.49	+35:25:39.4	1.070	A	B[13]	QSO: broad Mg II,[O II],broad Balmer lines
WISE AGN	14:32:37.33	+35:25:12.6	1.117	A	B[01]	Mg II absorption,[O II],D4000
MIPS	14:32:38.38	+35:21:54.2	0.495	A	B[17]	[O II],Hβ,[O III]
IRAC AGN	14:32:39.41	+35:23:45.0	1.979	B	B[11]	QSO: Mg II
serendip	14:32:39.81	+35:21:55.6	0.835	B	B[10]	[O II]
IRAC AGN	14:32:40.04	+35:21:54.5	0.543	A	B[10]	BL AGN: lots of lines
MIPS	14:32:41.29	+35:26:04.5	0.071	A	B[25]	Hβ,[O III],Hα
MIPS	14:32:45.09	+35:23:23.4	0.601	A	B[22]	[O II],Hβ

Note. — Spectroscopic measurements for 129 additional sources. Coordinates shown are in J2000. Q indicates the quality of the redshift (see §4.4 for details). Masks A, B and C were observed with DEIMOS, and the bracketed numbers indicate the DEIMOS slitlet number. Mask F was observed with LRIS.